

## Impacts of rock components on the competitive adsorption of carbon dioxide and methane in organic shales

Ibrahim Gomaa, Isa Silveira de Araujo, Zoya Heidari <sup>\*</sup>, D. Nicolas Espinoza

Hildebrand Department of Petroleum and Geosystems Engineering, The University of Texas at Austin, Austin, TX, 78712, USA

### ABSTRACT

The competitive adsorption of CO<sub>2</sub> and CH<sub>4</sub> on kerogen and clay surfaces significantly affects CO<sub>2</sub> sequestration and enhanced gas recovery (EGR) in organic shale-gas reservoirs. Conventional laboratory methods struggle to quantify individual gas adsorption in CO<sub>2</sub>:CH<sub>4</sub> mixtures. To address this challenge, we aim to quantify (a) the effects of kerogen type, pore structure, and thermal maturity on CO<sub>2</sub>:CH<sub>4</sub> competitive adsorption, (b) the impact of clay surface chemistry on the adsorption capacity of organic shale formations, and (c) the influence of different moisture and oil contents on the adsorption capacity of kerogen and clay structures. We used Grand Canonical Monte Carlo (GCMC) simulations (verified against previously documented experimental measurements) to investigate how kerogen composition, pore structure, and thermal maturity, water/oil saturation, and clay surface chemistry influence CO<sub>2</sub> adsorption under reservoir conditions.

Results suggest that changing kerogen from type I to III increases CO<sub>2</sub> adsorption from 1.42 mmol/g to 5.56 mmol/g at 330 K and 20 MPa. Increasing thermal maturity significantly affected CO<sub>2</sub> adsorption, though raising reservoir pressure from 1 MPa to 20 MPa reduces CO<sub>2</sub>:CH<sub>4</sub> selectivity. Moreover, the presence of moisture and oil decrease maximum CO<sub>2</sub> adsorption. For clay minerals, the positively charged K-illite enhances CO<sub>2</sub> adsorption by 133 % compared to negatively charged illite and exhibits a CO<sub>2</sub>/CH<sub>4</sub> selectivity of 17.2 versus 1.48 in kaolinite. These findings emphasize that reservoir conditions as well as composition critically affect adsorption capacity and selectivity. The introduced molecular simulation framework enabled extensive sensitivity analyses of factors influencing CO<sub>2</sub> storage at conditions that extend beyond the reach of conventional laboratory experiments, which potentially enables the optimization of CO<sub>2</sub> storage strategies in organic shale-gas reservoirs.

### 1. Introduction

Organic shale is a sedimentary rock with a high content of organic matter that varies in compositional properties and concentration depending on the depositional environment. The amount of organic matter in organic shale can vary significantly, reported within the range of 5–65 % (Forsman and Hunt, 1958; Duncan and Swanson, 1966; Myers and Wignall, 1987). The organic matter consists of solid material known as “kerogen”, minor amounts of bitumen, oil, and hydrocarbon gas. The remaining constituents of organic shale are clay minerals, and smaller amounts of quartz, feldspar, and calcite. Natural gas exists in the tight and organic shale reservoirs in three states: free gas in natural fractures, adsorbed gas in matrix, and absorbed/dissolved gas in kerogen and bitumen (Du and Nojabaei, 2019). The production decline from organic shale-gas reservoirs due to pressure depletion is a significant challenge facing the oil and gas industry. To address this challenge, the implication of EGR techniques, such as CO<sub>2</sub> injection is required.

CO<sub>2</sub> injection and storage are effective methods for enhancing hydrocarbon recovery in shale-gas reservoirs. Since CO<sub>2</sub> has an adsorption preference in shale reservoirs over methane, it can be trapped in the pores

of the rock by sorption. This process liberates the trapped methane and increase its flow rate after primary depletion (Busch et al., 2008). This high adsorption selectivity for organic shale formations towards CO<sub>2</sub> makes them potential candidates for CO<sub>2</sub> sequestration projects as well. CO<sub>2</sub> storage in organic shale-gas reservoirs involves a complex interplay of trapping mechanisms. The main ones include structural trapping, dissolution trapping, and adsorption trapping (Soltanian et al., 2017; Iglauer, 2018; Mohagheghian et al., 2019). The main focus of this paper is to investigate the factors affecting CO<sub>2</sub> adsorption trapping in organic shale-gas reservoirs either during EGR operations or during a carbon sequestration project.

Laboratory experiments can be used to characterize the adsorption capacity of organic shale formations as well as their pure solid constituents such as kerogen and clay minerals (Busch et al. 2008, 2016; Chen and Lu, 2015; Niu et al., 2018; Hamza et al., 2021; Gomaa et al., 2023a). Busch et al. (2008) carried out diffusive transport and gas sorption experiments on Muderong shale and different clay minerals to study the CO<sub>2</sub> sealing integrity and sorption capacity of these materials. The authors claimed various trapping mechanisms that contributed to the CO<sub>2</sub> storage in shale reservoirs including aqueous solubility, geochemical

\* Corresponding author.

E-mail address: [zoya@austin.utexas.edu](mailto:zoya@austin.utexas.edu) (Z. Heidari).

interactions, and physisorption. Moreover, they demonstrated that the high CO<sub>2</sub> sorption capacity of Muderong shale is attributed to the high adsorption capacity of its clay content. However, their experimental methods provided macro-scale data on CO<sub>2</sub> sorption but lack atomistic details of the interaction mechanisms at the mineral-water interface. Kang et al. (2011) experimentally investigated CO<sub>2</sub> sequestration in organic-rich shales. They found that up to 97 % of CO<sub>2</sub> is stored in the organic pores by the adsorption mechanism. However, the impact of oil and water saturations on the CO<sub>2</sub> diffusion and adsorption capacity of the tested samples are yet to be quantified. The latter can be a challenging task due to the complexity of saturating the rock sample during the manometric adsorption experiments adopted in previous publications.

Heller and Zoback (2014) tested the competitive adsorption of CO<sub>2</sub> and CH<sub>4</sub> gases on shale, clay, and activated carbon samples at 40 °C. They showed that the CO<sub>2</sub> adsorption capacity of shale samples increased with an increase in their TOC. Meanwhile, the outcomes of their results suggested that composition affects adsorption but cannot explain the atomistic-level interactions between the shale matrix and the gases. Moreover, the authors hypothesized about the influence of water content, but cannot directly probe this in their measurements. To the best of the authors' knowledge, none of the aforementioned lab-scale experimental studies investigate the influence of different fluid saturation, the mineral geochemistry and surface properties including surface charges and chemical composition on the competitive adsorption of CO<sub>2</sub> and CH<sub>4</sub> in organic shales. The main reason is the limitation of the laboratory experiments to the bulk interactions between the adsorbate gases and the tested rock samples.

One of the parameters that controls the efficacy of CO<sub>2</sub> trapping by adsorption while CH<sub>4</sub> is being liberated during the EGR projects is the CO<sub>2</sub>/CH<sub>4</sub> adsorption selectivity. Several factors affect the surface selectivity of CO<sub>2</sub> over CH<sub>4</sub> in organic shales, including mineralogy, composition and concentration of organic matter, pressure, temperature, and adsorption history (Niu et al., 2018; Zhou et al., 2019; Liu and Hou, 2020; Wang et al., 2021; Xie et al., 2021). Liu et al. (2019) evaluated the CO<sub>2</sub>/CH<sub>4</sub> adsorption selectivity in organic-rich shale samples using low-field NMR experiments. They reported that the CO<sub>2</sub>/CH<sub>4</sub> adsorption selectivity in the tested samples varies between 3.43 and 5.81 depending on the CO<sub>2</sub>/CH<sub>4</sub> pressure. However, the results did not explain the contribution of rock composition to the adsorption selectivity. For instance, the presence of clay minerals, such as illite, can increase the adsorption of CO<sub>2</sub> relative to CH<sub>4</sub> due to its polar surfaces and cation exchange capacity (Chen and Lu, 2015; Busch et al., 2016; Hamza et al., 2021). Moreover, organic matter in organic-rich shales acts as an adsorption site for both CO<sub>2</sub> and CH<sub>4</sub>, while the selectivity between the two gases is influenced by the type and thermal maturity of organic matter (Zhang et al., 2012; Huang et al., 2018a; Wang et al., 2018). Since laboratory-scale experiments usually focus on the bulk rock-fluid interactions, there is a need for a finer scale of investigation to quantify the impacts of the aforementioned factors on CO<sub>2</sub>/CH<sub>4</sub> competitive adsorption selectivity.

Molecular dynamics simulations can help understand and quantify the influence of the constituents in a given organic shale reservoir, such as kerogen, clay minerals, oil, and water content, on the CO<sub>2</sub>:CH<sub>4</sub> adsorption/desorption process (Huang et al., 2018b; Kang et al., 2020; Wang et al., 2018; Zhang et al., 2012). Obliger et al. (2018) quantified the self-diffusivities of light alkanes of C ≤ 12 in different kerogen structures of varying types and thermal maturity levels. However, they did not investigate the impact of these alkanes on gas adsorption. On the other hand, Bonnaud et al. (2023) used kerogen type IID to model the competitive adsorption and diffusion of CH<sub>4</sub>/CO<sub>2</sub> mixtures in mature organic matter without addressing the impact of different kerogen types or thermal maturity levels on the gas adsorption. Yuan et al. (2022) included different kerogen models of different types and thermal maturity levels to evaluate the diffusion and sorption behavior of CO<sub>2</sub> and CH<sub>4</sub> mixtures in organic-rich mudrocks under different moisture

content. Furthermore, Hu et al. (2019) developed molecular models for illite, kaolinite, and montmorillonite to evaluate the competitive sorption of CH<sub>4</sub> and CO<sub>2</sub> on clay surfaces. However, a comprehensive study of the impacts of different clay minerals and kerogen structures in the presence of reservoir fluids on CO<sub>2</sub>:CH<sub>4</sub> competitive adsorption is still missing.

The objective of this paper is to adopt molecular simulations to quantify the influence of kerogen type and thermal maturity on the competitive adsorption of CO<sub>2</sub> and CH<sub>4</sub> under various conditions of pressures and temperatures. Moreover, we carry out a sensitivity analysis on the influence of the clay surface charge on the adsorption selectivity of the CO<sub>2</sub>:CH<sub>4</sub> under different temperatures. Finally, we quantify the impacts of moisture and oil content on the CO<sub>2</sub> storage capacity of organic shale-gas formations. The novelty of this work lies in quantifying the impact of reservoir fluids, the geochemistry of organic matter (i.e., kerogen types and thermal maturity) and clay minerals on the CO<sub>2</sub>:CH<sub>4</sub> competitive adsorption under various reservoir pressure and temperature conditions. Moreover, the molecular-scale simulations have been validated against available previously documented experimental results to ensure reliability. We also provide practical field-scale applications for the findings derived from the resulting adsorption results. This level of investigation using molecular dynamic simulations enables understanding the interactions between CO<sub>2</sub> and the rock and fluid components of organic shale reservoirs. This leads to enhanced selection of best reservoir candidates for CO<sub>2</sub> sequestration and EGR applications.

## 2. Methods

We developed molecular kerogen structures of different types (i.e., IA, IIA, and IIIA) and different thermal maturity levels within type IIA (i.e., IIA, IIB, IIC, and IID). In addition, we modeled kaolinite and illite clay structures with different surface polarization characteristics. Then, we used the grand canonical Monte Carlo ensemble to evaluate the CO<sub>2</sub>:CH<sub>4</sub> competitive adsorption isotherms over the developed kerogen and clay structures. We finally evaluated the impacts of moisture and oil content on the CO<sub>2</sub> adsorption capacity for both kerogen and clay structures.

### 2.1. Development of realistic molecular structures of kerogen

Ungerer et al. (2015) provided the basic kerogen molecular units that represent the actual chemical structure of the realistic kerogen samples of different types and thermal maturity levels. The composition and chemical structure of these kerogen models were built to match the basic elemental analysis, aromaticity level, and functional group data measured using X-ray photoelectron spectroscopy (XPS) and <sup>13</sup>C NMR (Kelemen et al., 2007). Ungerer et al. (2015) listed the chemical composition of the kerogen structures along their H/C and O/C ratios as well as the various present functional groups. Fig. 1 shows the Van Krevelen diagram that classifies the kerogen structures based on their H/C and O/C ratios into different types and different thermal maturity levels.

From each kerogen model, we built dense kerogen structures through an annealing process. The annealing process was carried out in the LAMMPS software where the atomic interaction parameters between the kerogen atoms were adopted from the consistent-valence forcefield (CVFF) (Dauber-Osguthorpe et al., 1988). Jagadisan and Heidari (2022) and Araujo et al. (2023) used CVFF to successfully model kerogen structures. Moreover, CVFF is widely used to model the atomic interactions of organic materials (Heinz et al., 2008; Abdalla et al., 2018). The total potential energy of the system (*E*) in CVFF is expressed as

$$E_{ij} = 4e_{ij} \left[ \left( \frac{\sigma_{ij}}{r} \right)^{12} - \left( \frac{\sigma_{ij}}{r} \right)^6 \right] + \frac{Cq_i q_j}{\epsilon r} + K_r(r - r_0)^2 + K_\theta(\theta - \theta_0)^2 + K_\phi[1 + d \cos(n\phi)], \quad (1)$$

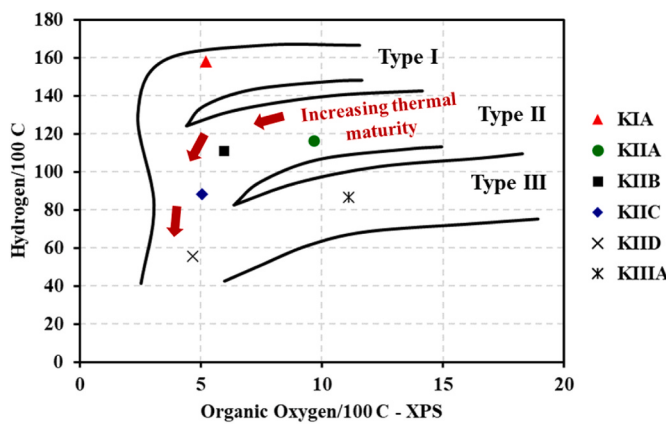


**Fig. 1.** Van Krevelen diagram illustrating the three main types of organic matter (i.e., KIA, KIIA, and KIIIA) as well as the evolution path for KIIA towards its corresponding mature models: KIIB, KIIC, and KIID (modified after Kelemen et al. (2007) and Ungerer et al. (2015)).

where  $r$  is the distance between two interacting atoms,  $\varepsilon$  is the depth of the potential well, and  $\sigma$  is the distance at which the atom-atom potential energy is zero. In the Coulombic equation (second component of the defined equation)  $C$  parameter is an energy-conversion constant,  $q_i$  and  $q_j$  are the charges on the two atoms, and  $\epsilon$  is the dielectric constant. In the harmonic component,  $K_r$ ,  $K_\theta$ , and  $K_\phi$  are the harmonic constants for the bonds, angles, and dihedrals potentials, respectively.  $r_0$ ,  $\theta_0$ , and  $\varphi_0$  represent equilibrium distance/angle constant for the bonds, angles, and dihedrals potentials, respectively. For unlike atomic species, Lorentz-Berthelot combining rules are used to calculate the cross Lennard-Jones (LJ) parameters via

$$\sigma_{ij} = \frac{\sigma_{ii} + \sigma_{jj}}{2}, \quad (2)$$

and

$$\varepsilon_{ij} = \sqrt{\varepsilon_{ii} \times \varepsilon_{jj}}. \quad (3)$$

The annealing process started by packing four kerogen molecules in a large cubic cell of a volume of  $1000 \text{ nm}^3$  to avoid any overlapping between the kerogen atoms. Then, the temperature of the system was stabilized in the Canonical ensemble at  $900 \text{ K}$  for  $200 \text{ ps}$ . After that, the kerogen structures went through four successive simulations in the isothermal-isobaric ensemble at  $900 \text{ K}$ ,  $700 \text{ K}$ ,  $500 \text{ K}$ , and  $300 \text{ K}$  under a pressure of  $200 \text{ bar}$ . A time step of  $0.001 \text{ ps}$  was used to capture the changes in the system during the different simulation stages that lasted for  $1200 \text{ ps}$ . This led to stabilizing the kerogen density around  $1.05\text{--}1.26 \text{ g/cc}$  which matched the actual kerogen density (Dang et al., 2016). Fig. 2 shows the final kerogen structures used in this paper. The kerogen structures are assumed to be rigid as we do not account for the  $\text{CO}_2$ -induced swelling. This provides a controlled comparison across different kerogen models, enabling clearer attribution of adsorption trends to chemical and structural differences rather than deformation effects.

## 2.2. Development of clay structures with different surface charges

We represented the clay content of organic shales with kaolinite and illite structures. The kaolinite clay structure has a chemical formula of  $\text{Al}_2\text{Si}_2\text{O}_5(\text{OH})_4$ . Kaolinite, in nature, has a layered structure consisting of one tetrahedral sheet and one octahedral sheet stacked on top of each other. The tetrahedral sheet is composed of four oxygen atoms surrounding a silicon atom in the center, while the octahedral sheet is composed of six hydroxyl groups surrounding an aluminum ion in the center. The tetrahedral and octahedral sheets are linked together through oxygen atoms, forming a two-dimensional layer of atoms.

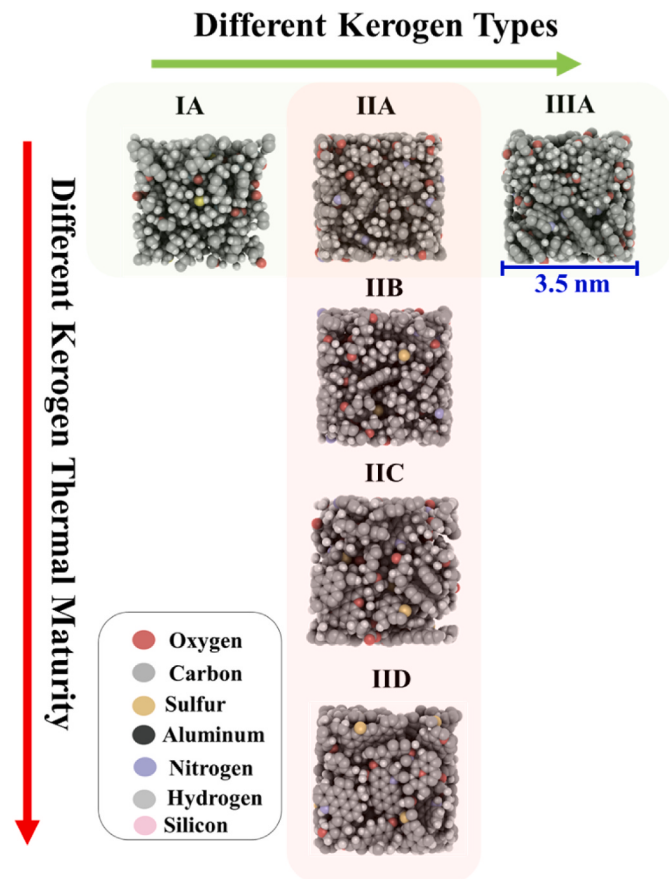


**Fig. 2.** The developed kerogen models of different types and thermal maturity levels.

Adjacent layers are held together through weak van der Waals forces, resulting in a three-dimensional structure (Frost and Kristof, 2004; Araujo and Heidari, 2022). Clay Force Field (CLAYFF) developed by (Cygani et al., 2004) was used to describe the interactions between the different clay atoms. In this paper, the developed kaolinite structure has a neutral surface without any added surface charges. Fig. 3a shows the developed kaolinite structure. A unit kaolinite cell developed by Bish (1993) was used to construct the kaolinite pore structure by replicating the unit cell in the x and y directions with maintaining periodic boundary conditions. The final kaolinite structure has two parallel sheets with a pore size of  $2 \text{ nm}$ .

The illite clay structure is formed by a pyrophyllite unit cell structure that is a 2:1 electrically neutral clay sheet. The basic structure of illite consists of two layers; the tetrahedral layer and the octahedral layer. The tetrahedral layer is made up of four oxygen atoms surrounding a silicon or aluminum ion at the center. The octahedral layer is made up of six oxygen atoms forming a slightly distorted octahedron that encloses a magnesium, iron, or aluminum ion. The tetrahedral and octahedral layers alternate to form a 2:1 layered structure, with the octahedral layer sandwiched between two tetrahedral layers. To mimic the negative surface charge of illite in nature, the neutral structure went through an isomorphic substitution where one silicon (Si) atom is substituted by an aluminum (Al) atom as demonstrated in Fig. 3b. However, in the presence of formation water, potassium cations tend to adhere to the illite surface to neutralize its surface charge and increase its CEC as demonstrated in Fig. 3c. The final chemical formula of the developed K-illite unit cell is  $\text{K}[\text{Si}_7\text{Al}] \text{Al}_4\text{O}_{20}(\text{OH})_4$ . Illite sheets are then constructed by replicating the unit cell in the x and y directions assuming periodic boundary conditions. Two parallel illite sheets are used to create a slit-like pore structure with a pore size of  $2 \text{ nm}$ . The pore size of the clay

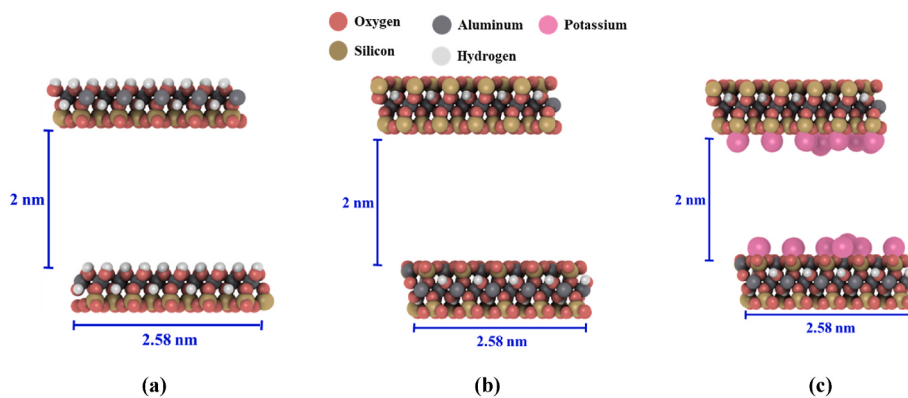


**Fig. 3.** The developed clay structures including (a) kaolinite, (b) illite with negative surface charge, and (c) K-illite with positive K-ions attached to the illite surface.

structures is maintained constant throughout the simulation to eliminate the effect of clay swelling on the adsorption results, allowing isolation of the influence of the clay surface charge on its surface adsorption.

### 2.3. Evaluation of CO<sub>2</sub>:CH<sub>4</sub> competitive adsorption isotherms using grand canonical Monte Carlo (GCMC) simulations

GCMC simulation is a widely used computational method in the field of gas adsorption to study the adsorption behavior of pure gases and their mixture in porous materials (Sirjoosinh et al., 2010; Gomaa et al., 2023a, 2023b, 2023c). In these simulations, the adsorption of gas molecules in a porous material is modeled by introducing a hypothetical gas reservoir at a fixed temperature and pressure. The GCMC simulation method allows the simulation of the adsorption process at equilibrium, where the number of adsorbed gas molecules and the gas pressure are in balance between the gas reservoir and the porous material. The probability of a gas molecule being adsorbed at a particular site in the porous material is calculated by using the grand canonical partition function, which is a function of the temperature, pressure, and chemical potential of the gas molecules. The GCMC simulation method can be used to investigate various aspects of gas adsorption, such as the adsorption isotherms, which describe the amount of gas adsorbed as a function of the gas pressure, and the selectivity of the porous material towards different gas molecules. This method can also be used to investigate the effect of temperature, pressure, and other variables on the adsorption behavior of gases in porous materials (Peng et al., 2009; Sirjoosinh et al., 2010; Xiong et al., 2017).

The CO<sub>2</sub>:CH<sub>4</sub> adsorption selectivity (*S*) gives information about the preference of the adsorbent structure to selectively adsorb CO<sub>2</sub> gas over CH<sub>4</sub> while they compete with each other in a gas mixture. In practice, when comparing the adsorption of CO<sub>2</sub> and CH<sub>4</sub> for enhanced gas recovery applications, higher values of selectivity (*S* > 1) indicate that the adsorbent preferentially adsorbs CO<sub>2</sub> over CH<sub>4</sub>. Conversely, selectivity values less than 1 (*S* < 1) indicate that the adsorbent preferentially adsorbs CH<sub>4</sub> over CO<sub>2</sub>. The higher the selectivity, the more effective the adsorbent is at separating CO<sub>2</sub> from CH<sub>4</sub>. This selectivity parameter can be calculated via

$$S = \frac{x_{CO_2}/x_{CH_4}}{y_{CO_2}/y_{CH_4}} \quad (4)$$

Where  $x_{CO_2}$  and  $x_{CH_4}$  are the average mole fraction of CO<sub>2</sub> and CH<sub>4</sub> in the adsorbed phase while  $y_{CO_2}$  and  $y_{CH_4}$  are the average mole fraction of CO<sub>2</sub> and CH<sub>4</sub> in the bulk phase.

We used the RASPA code developed by Dubbeldam et al. (2016) to run the GCMC simulations to evaluate the competitive adsorption of CO<sub>2</sub>:CH<sub>4</sub> gases in the developed kerogen and clay structures. We assigned 1,000,000 initialization cycles to the simulation in order to reach equilibrium conditions followed by 2,000,000 cycles for

production where the sorption values are reported. Different probabilities were assigned to MC moves of translation (50 %), regrowth (50 %), and identity change (100 %) between the two gas species trying to match the actual competitive adsorption of CO<sub>2</sub>:CH<sub>4</sub> in porous structures. A wide range of pressure values (i.e., 0–20 MPa) was used to construct the adsorption isotherms at each specific temperature of 330 K, and 400 K. These conditions are representative of supercritical CO<sub>2</sub> phase, aligning well with typical CO<sub>2</sub> sequestration scenarios in depleted gas reservoirs. Force fields were used to describe the interactions among the adsorbate gas molecules and between the gas molecules and the kerogen structures. In this paper, the Transferable Potentials for Phase Equilibria – Explicit Hydrogen (TraPPE - EH) force field was used to assign the interaction parameters between the CO<sub>2</sub> and CH<sub>4</sub> molecules (Potoff and Siepmann, 2001).

### 2.4. Quantification of the impacts of moisture and oil content on the CO<sub>2</sub> storage capacity of organic shale formations

Water and oil content is a critical parameter that affects the CO<sub>2</sub> adsorption capacity of both kerogen and clay structures that form the organic shale formations. In order to quantify the impact of water and oil content on the CO<sub>2</sub> storage capacity of the modeled kerogen and clay structures, we developed various simulation cases with different water and oil content. The water and oil contents were calculated as a weight fraction of the kerogen and clay structures (i.e., 1 wt%, 2 wt%, and 3 wt %). Water molecules were represented by the Transferable Intermolecular Potential with 3 Points (TIP3P) model, which represented each water molecule as a rigid molecule with three interaction sites: two hydrogen atoms and one oxygen atom. The interactions between the water molecules were described by the Lennard-Jones potential and Coulombic interactions. Meanwhile, the oil content was represented by the decane (C<sub>10</sub>H<sub>22</sub>) as a linear chain alkane. In the case of the interaction of decane molecules, we used the Optimized Potential for Liquid Simulations United-Atom (OPLS-UA) force field, which is a well-established force field for simulating organic molecules (Siu et al., 2012; Jorgensen and McDonald, 1998; Ulmschneider and Ulmschneider, 2009). This force field represents each atom in the decane molecule as a point charge and describes the interactions between the atoms using a combination of bonded and non-bonded interactions. The bonded interactions include covalent bonds, angles, and dihedrals, while the non-bonded interactions include van der Waals interactions and Coulombic interactions. Using OPLS-UA to model decane as a coarse-grained model helps to accelerate the simulations by reducing the number of degrees of freedom while maintaining a good accuracy for adsorption calculations. The water and oil molecules are then inserted into the kerogen and clay pores with the corresponding saturation before running the GCMC simulations.

### 3. Results

#### 3.1. Validation of the force field parameters

To validate the force field parameters used in modeling gas behavior within kerogen and clay nanopores, we compared the simulated gas densities obtained under various pressures and temperature values against reference densities calculated from the National Institute of Standards and Technology (NIST) database using the equation of state (EOS). Fig. 4 illustrates this comparison, including the average absolute percentage error (AAPE) to quantify deviations between simulation results and NIST values. The simulated gas densities closely match the NIST data, showing a maximum AAPE of 3.37 % for CO<sub>2</sub> at 330 K. Notably, deviations occur primarily at pressures above 10 MPa. This comparison confirms the reliability and accuracy of the selected force field parameters for modeling gas behavior in kerogen and clay nanopores.

#### 3.2. Estimation of pore volume and surface area in kerogen and clay minerals

Kerogen pore volume fraction can be defined as the empty space of

the structure divided by the total volume. Experimentally, pore volume can be measured at room temperature using helium gas due to its low sorption tendency on the kerogen surface. In the developed molecular models, we quantified the kerogen pore volume using the Widom particle insertion as it corresponds to the new Rosenbluth weight (Widom, 1963). Fig. 5 shows the results of the available pore volume fraction for each kerogen structure as a function of the Hydrogen:Carbon (H/C) ratio. The size of the circles in the plot indicates the relative O/C ratio for each kerogen structure. We observe that increasing kerogen thermal maturity leads to an increase in its available pore volume fraction. This is attributed to the high H/C ratios found in the low thermally mature kerogen structures (e.g., kerogen IA). With increasing thermal maturity, kerogen aromaticity increases, and the H/C ratios decrease leading to form polycyclic aromatic structures with wide pore spaces for over-mature kerogen. Kerogen structures with higher pore volumes are expected to adsorb and store more CO<sub>2</sub> gas.

The surface areas of the simulated structures are estimated by rolling a nitrogen gas atom over the surface of the structure at a temperature of 300 K. Nitrogen gas is used to mimic the BET surface area lab measurements that use nitrogen gas sorption. However, the surface area of the tested molecular structures in this paper is calculated numerically using the Shrake-Rupley algorithm (Shrake and Rupley, 1973). The

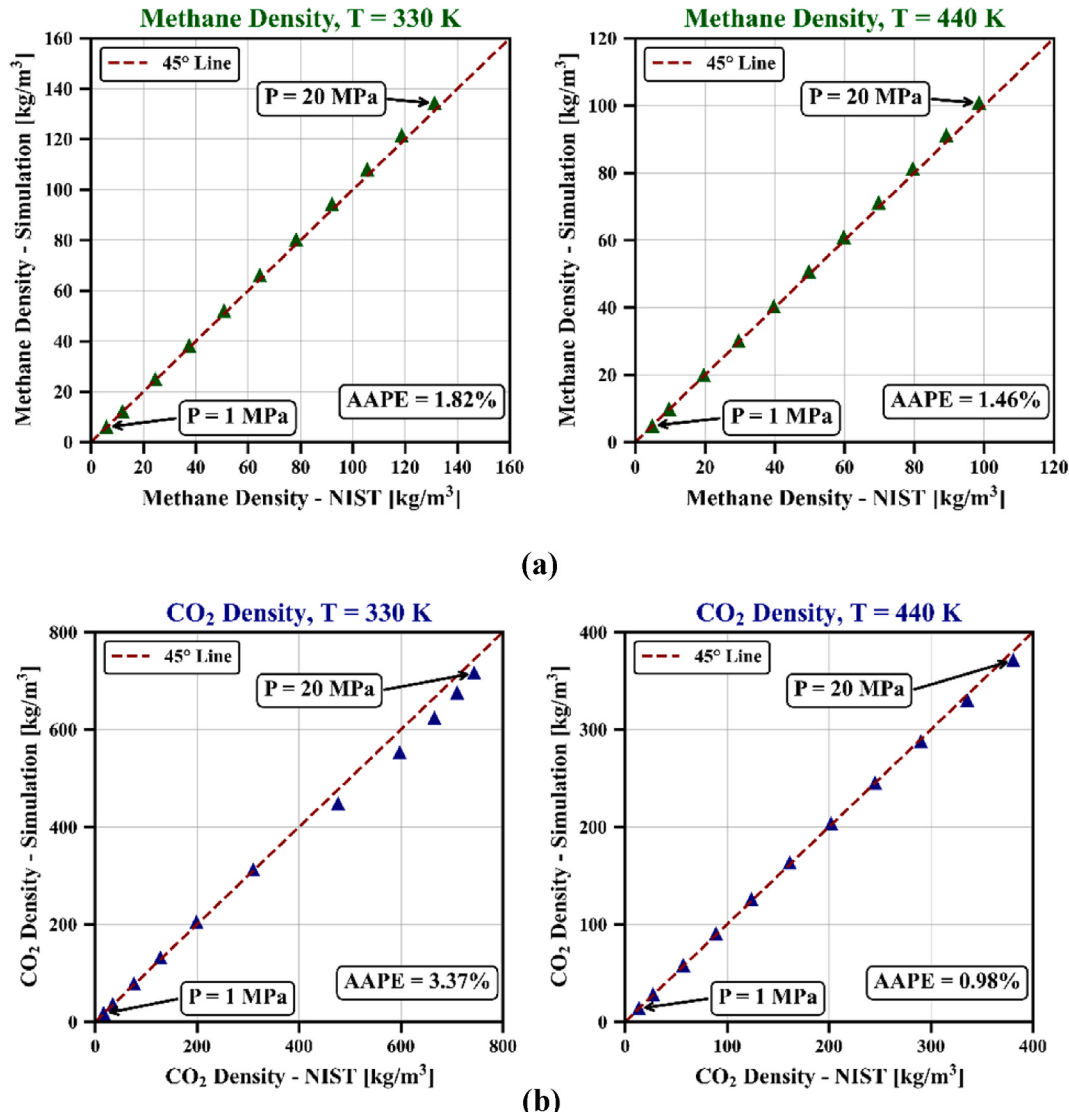


**Fig. 4.** Validating the results of the force filed parameters for (a) methane and (b) CO<sub>2</sub> by comparing the gas bulk density from the molecular simulations to the ones from NIST database.

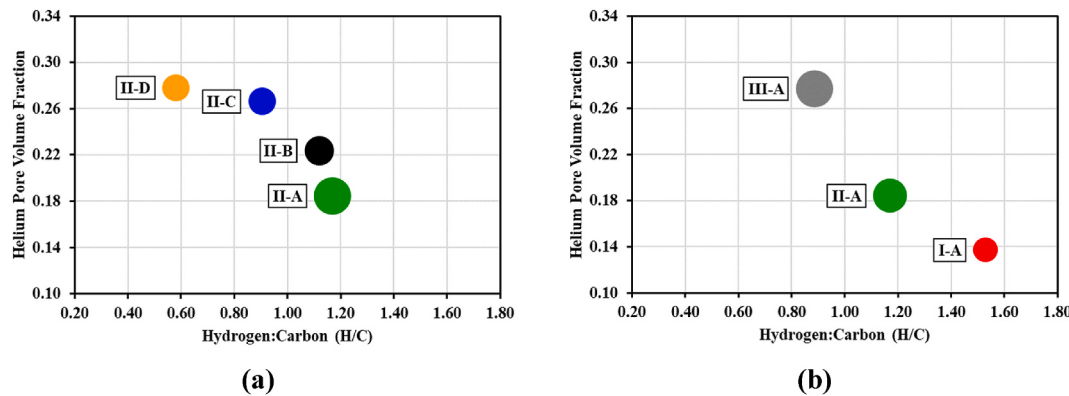
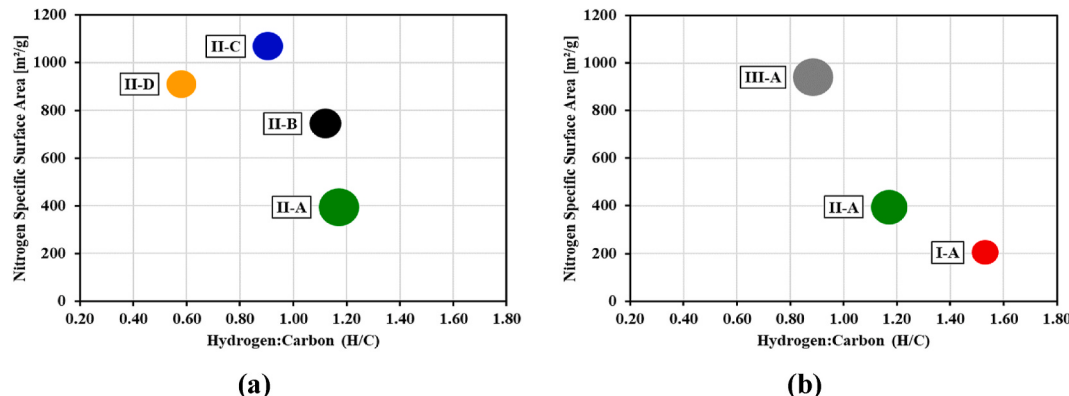


**Fig. 5.** The helium void fraction of the kerogen structures estimated using the Widom particle insertion technique as a function of the H/C ratio for (a) kerogen type II of different thermal maturity levels and (b) different kerogen types. The size of the circles indicates the relative O/C ratio for each kerogen structure.

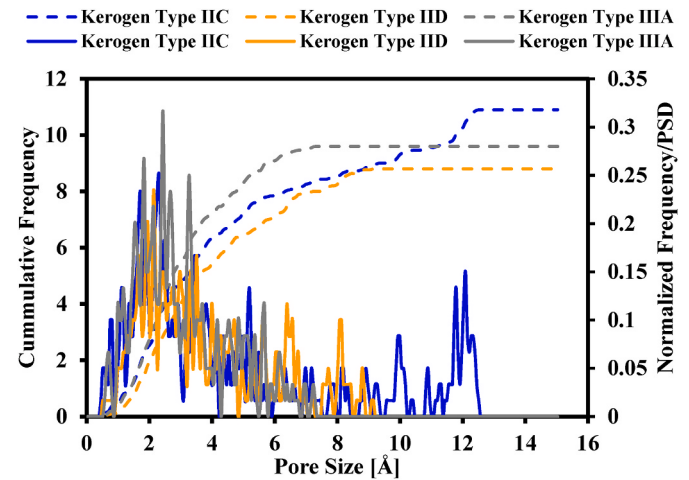
aforementioned algorithm solves for the accessible surface area of the structure by drawing a mesh of equidistant points around the structure atoms. This equidistance equals the van der Waals radius of a nitrogen molecule which is 0.155 nm (Bondi, 1964). The total overlap between all mesh portions is then multiplied by the area of the nitrogen atom to calculate the total surface area of the structure. Therefore, the estimated surface area values in this paper can overestimate the reported values of the BET surface area measured at the lab. This is attributed to the difference in the measurement mechanisms as well as the scale of tested samples in the two techniques.

Fig. 6 (a) shows the specific surface area of kerogen structures of type II with various thermal maturity levels. We observe an increase in the kerogen surface area as the thermal maturity increases from type IIA to type IIC. Fig. 6 (b) shows the specific surface area of the three kerogen types (i.e., IA, IIA, and IIIA). We observe the relation between the increase in the kerogen thermal maturity through the reduction in the H/C ratio and the increase in the kerogen specific surface area. However, the values of surface areas of both kerogen IID and IIIA are less than kerogen IIC despite the fact that they both have higher void volume than IIC. This can be attributed to the inaccessible pore spaces inside these kerogen structures. Inaccessible pores prevent the nitrogen atom from rolling around their surface and create overlapped regions with the neighbor pores. Therefore, they are not included in the estimated total surface area of the structure. This can be explained by investigating the pore-size distribution (PSD) of kerogen IIC, IID, and IIIA.

Fig. 7 shows the PSD and its corresponding cumulative values of the aforementioned kerogen structures—IIC, IID, and IIIA. RASPA uses the method of Gelb and Gubbins (1999) to compute the PSD of the molecular structures. The kerogen structure of type IIC has a bimodal pore-size distribution with a high local maxima of around 12 Å. On the other



**Fig. 6.** The specific surface area estimated using nitrogen gas atom as a function of the H/C ratio for (a) kerogen type II of different thermal maturity levels and (b) different kerogen types. The size of the circles indicates the relative O/C ratio for each kerogen structure.



**Fig. 7.** The pore-size distribution of kerogen types IIC, IID, and IIIA.

hand, kerogen of types IID and IIIA have unimodal pore-size distributions with the majority of pore sizes being less than 5 Å. This explains why kerogen type IIC has a larger surface area than kerogen types IID and IIIA, while it has a smaller pore volume. The bimodal nature of the PSD of kerogen type IIC matches the experimental results documented by Ansari et al. (2022).

### 3.3. Impact of kerogen types on the CO<sub>2</sub>:CH<sub>4</sub> competitive adsorption in organic shale formations

In order to evaluate the impact of the different kerogen types (i.e., IA, IIA, and IIIA) on the competitive adsorption of both CO<sub>2</sub> and CH<sub>4</sub>, we simulated a hypothetical gas reservoir with an equimolar fraction of CO<sub>2</sub> and CH<sub>4</sub>. Then, we allowed the gas to get adsorbed to the kerogen surface based on the favorable thermodynamic status of the system. Fig. 8 shows the adsorption isotherms of CO<sub>2</sub> and CH<sub>4</sub> components associated with kerogen types IA, IIA, and IIIA at temperatures of 330 K and 400 K for a pressure range of 0–20 MPa. The results show that CO<sub>2</sub> gas has more affinity to get adsorbed to all the kerogen types compared to CH<sub>4</sub>. Moreover, among the kerogen types, type IIIA exhibits the highest adsorption capacity, followed by type IIA and type IA. This observation is attributed to the change in both the pore structure and the chemical structure of the kerogen models as we move from type IA to type IIIA. Kerogen IIIA has more aromatic carbon structures than both kerogen types IIA and IA (Ungerer et al., 2015). This makes the pore volume of kerogen IIIA higher than the other two types giving more space for the gas species to get stored and adsorbed to the kerogen surface. Moreover, KIIIA features abundant aromatic structures interconnected by numerous oxygen-rich polar functional groups, such as hydroxyl, carboxyl, and carbonyl groups. The high aromaticity and presence of polar sites create strong adsorption affinity for CO<sub>2</sub> molecules. Additionally, Kerogen IIIA possesses a larger micropore volume compared to the aliphatic-rich Type I kerogen or moderately aromatic Type II kerogen. Meanwhile, increasing the temperature from 330 K to 400 K leads to a decrease in the total adsorption capacity for both gases. This is attributed to the exothermic nature of the CO<sub>2</sub> and CH<sub>4</sub> adsorption process.

Fig. 9 highlights the maximum adsorption capacities of kerogen types IA, IIA, and IIIA for CO<sub>2</sub> and CH<sub>4</sub> at 20 MPa across temperatures of 330 K and 400 K. The data reveals that increasing the temperature significantly reduces CO<sub>2</sub> adsorption across all kerogen types, with relative reductions of 38.3 %, 37.55 %, and 34 % for kerogen types IA, IIA, and IIIA, respectively. Similarly, the CH<sub>4</sub> adsorption capacities also decrease with temperature, but the reductions are less pronounced, showing decreases of 31.82 %, 25.62 %, and 16.23 % for kerogen types IA, IIA, and IIIA, respectively. This alignes with the results published by Ekundayo et al. (2021) as they reported a decrease in the CH<sub>4</sub> adsorption capacity of different shale samples to be within the range of 26.5 %–31 %, as temperature increased from 25 °C to 80 °C. However, this reduction can reach up to 50 % for some organic-rich shale samples as reported by Zou et al. (2017). Since we modeled kerogen as an amorphous porous structure, we can consider all the reported CO<sub>2</sub> uptake is in the sorption state inside the kerogen matrix and hence can be assumed as trapped CO<sub>2</sub> by sorption. It is worth noting that adsorption/desorption hysteresis due to kinetic trapping is generally not observable in GCMC simulations.

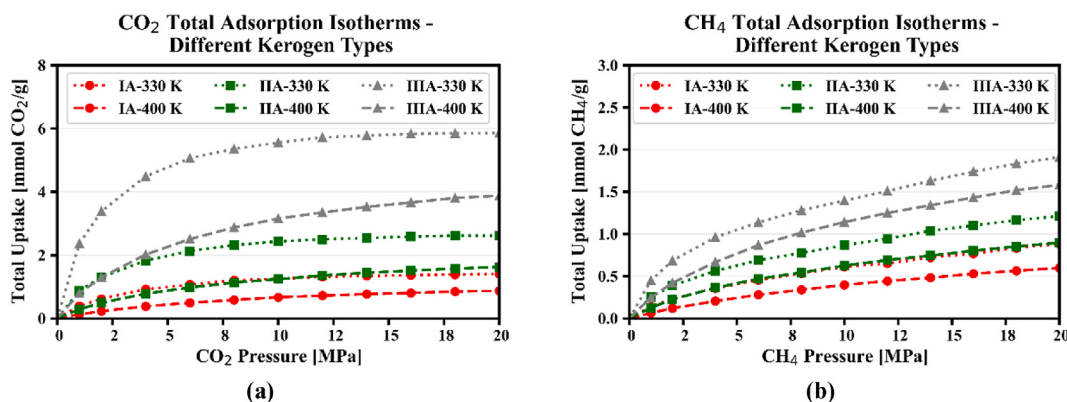


Fig. 8. The (a) CO<sub>2</sub> and (b) CH<sub>4</sub> competitive adsorption isotherms of kerogen types IA, IIA, and IIIA at temperatures of 330 K and 400 K, evaluated at a pressure range of 0–20 MPa.

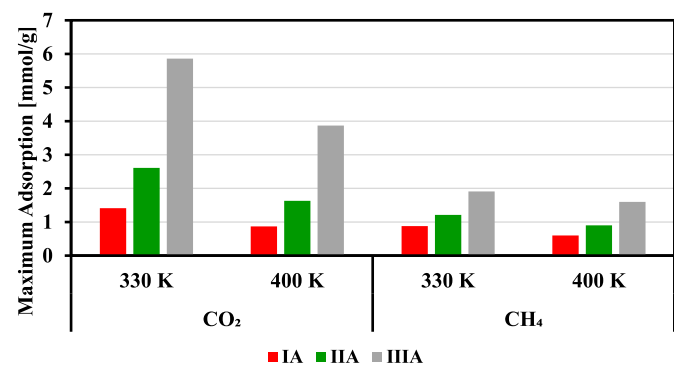


Fig. 9. The maximum adsorption capacity of kerogen types IA, IIA, and IIIA for both CO<sub>2</sub> and CH<sub>4</sub> at temperatures of 330 K and 400 K, evaluated at 20 MPa.

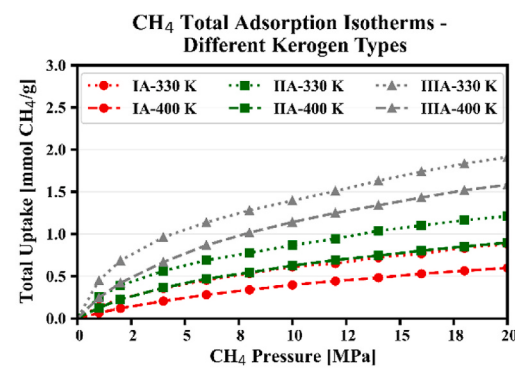
This is attributed to the fact that GCMC samples different configurations under equilibrium without accounting for diffusion-limited kinetics.

To quantify the binding energy between the adsorbate gases and the kerogen structures, we evaluated the adsorption-weighted average for the enthalpy of adsorption ( $\Delta H_{avg}$ ) over the pressure range 1–20 MPa for both 330 K and 400 K temperature conditions.  $\Delta H_{avg}$  is calculated via

$$\Delta H_{avg} = \frac{\sum_i (Q_i \cdot \Delta H_i)}{\sum_i Q_i}, \quad (5)$$

where i represents the pressure value at which we specify the amount of gas adsorbed ( $Q_i$ ) and the corresponding enthalpy of adsorption ( $\Delta H_i$ ) for each gas species in the system.

Fig. 10 shows the average enthalpy of adsorption weighted by the amount of gas adsorbed at the different pressures for 330 K and 400 K for different kerogen types of IA, IIA, and IIIA. The negative values of the enthalpy resembles the exothermic nature of the adsorption process inside the kerogen pores. For all kerogen types, we found that CO<sub>2</sub> has a higher binding energy with the kerogen structures more than CH<sub>4</sub> due to the stronger electrostatic interactions between CO<sub>2</sub> molecules and the various functional groups in the kerogen structures. This explains why CO<sub>2</sub> has higher adsorption affinity than methane within kerogen pores. Moreover, increasing the temperature from 330 K to 400 K, leads to lower enthalpy of adsorption as we have less gas molecules get sorbed on the surface of kerogen pores. Another relevant parameter that provides insight into the strength of the interaction between the gas adsorbate and the kerogen molecular structure is the isosteric heat of adsorption. While this property offers valuable information on adsorption energetics, its calculation involves additional thermodynamic analysis that falls beyond the scope of the present study. We plan to address this aspect in detail in a forthcoming publication.



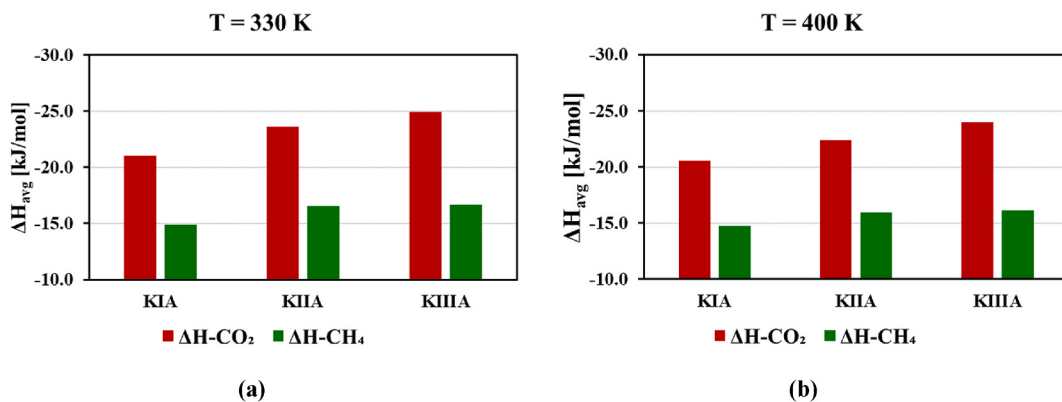


**Fig. 10.** The adsorption-weighted average of the enthalpy of adsorption for both  $\text{CO}_2$  and  $\text{CH}_4$  for kerogen types IIA, IIIA, and IIIA at temperatures of (a) 330 K and (b) 400 K.

#### 3.4. Impact of kerogen thermal maturity on the $\text{CO}_2:\text{CH}_4$ competitive adsorption in organic shale formations

The thermal maturation of kerogen is typically characterized by changes in the structure, chemical composition, and physical properties of the kerogen and the surrounding rock matrix. Therefore, quantifying the impact of kerogen thermal maturity on the  $\text{CO}_2:\text{CH}_4$  competitive adsorption is crucial for  $\text{CO}_2$  storage and enhanced gas recovery processes in shale-gas reservoirs. Fig. 11 shows the adsorption isotherms of  $\text{CO}_2$  and  $\text{CH}_4$  components associated with kerogen type II at different thermal maturity levels (i.e., IIA, IIB, IIC, and IID) at temperatures of 330 K and 400 K for a pressure range of 0–20 MPa. We observe that both  $\text{CO}_2$  and  $\text{CH}_4$  adsorption capacities increase with increase in the thermal maturity of kerogen. This observation is in agreement with the findings of Li et al. (2023) as they compared molecular-scale modelling results with methane adsorption experiments for kerogen types of different thermal maturity levels. This observation is attributed to the change in the kerogen structure with the increase in its thermal maturity. At low levels of thermal maturity, kerogen is primarily composed of large and complex organic molecules, such as aliphatic chains, aromatic rings, and heterocycles. As the temperature increases, these complex molecules break down into smaller and more volatile molecules, such as methane, ethane, propane, and butane (Alafnan et al., 2020). This increases the available pore volume for  $\text{CO}_2$  adsorption at highly mature kerogen structures (e.g., IID) compared to immature ones (e.g., IIA). Therefore, the maximum adsorption capacities of kerogen IID at 20 MPa are 86.20 % and 102.45 % higher than those of kerogen IIA at temperatures of 330 K and 400 K, respectively.

An increase in temperature from 330 K to 400 K leads to a decrease in

the total adsorption capacity for both  $\text{CO}_2$  and  $\text{CH}_4$ . Fig. 12 shows the maximum adsorption capacities of kerogen types IIA, IIB, IIC, and IID for  $\text{CO}_2$  and  $\text{CH}_4$  at 20 MPa at temperatures of 330 K and 400 K. The reductions in the  $\text{CO}_2$  maximum adsorption capacities due to temperature increase are 37.45 %, 34.86 %, 31.95, and 32.10 % for kerogen types IIA, IIB, IIC, and IID, respectively. Meanwhile, the reductions in the  $\text{CH}_4$  maximum adsorption capacities due to temperature increase are 25.62 %, 28.73 %, 27.31 %, and 15.73 for kerogen types IIA, IIB, IIC, and IID, respectively. Similar observations have been reported by Li et al. (2023) for the impact of increasing the temperature from 25 °C to 100 °C on the  $\text{CH}_4$  adsorption capacity of kerogen. This indicates that the  $\text{CO}_2$

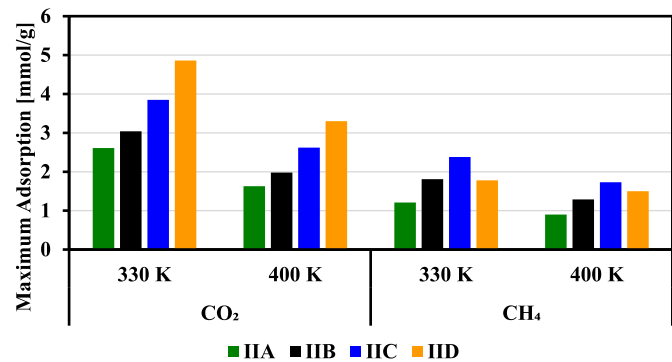


**Fig. 12.** The maximum adsorption capacity of kerogen type II with different thermal maturities (i.e., IIA, IIB, IIC, and IID) for both  $\text{CO}_2$  and  $\text{CH}_4$  at temperatures of 330 K and 400 K, evaluated at 20 MPa.

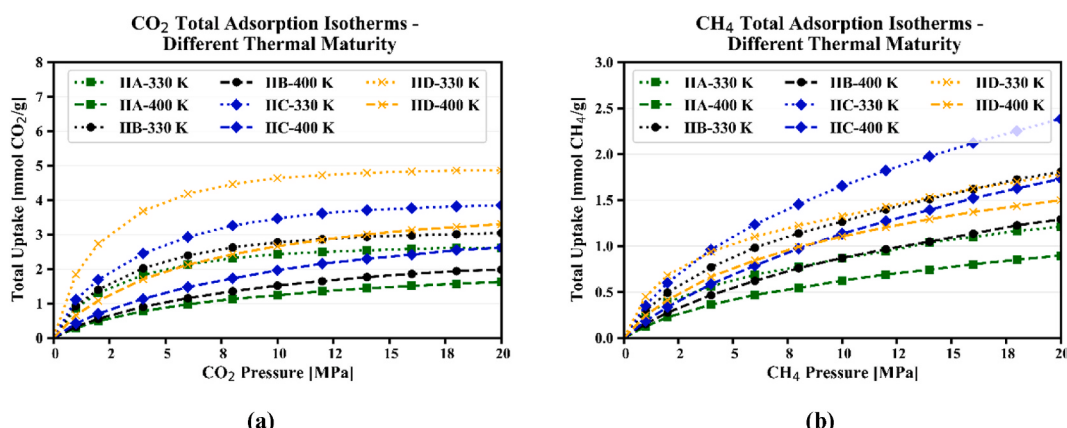


**Fig. 11.** The (a)  $\text{CO}_2$  and (b)  $\text{CH}_4$  competitive adsorption isotherms of kerogen types IIA, IIB, IIC, and IID at temperatures of 330 K and 400 K, evaluated at a pressure range of 1–20 MPa.

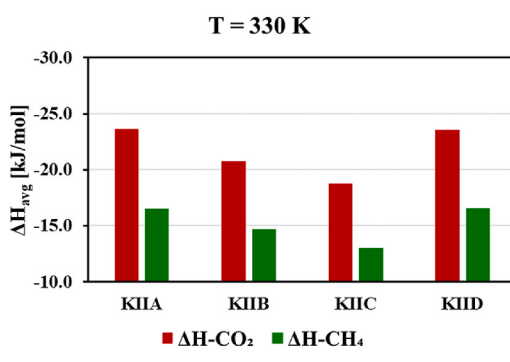
adsorption capacity is more sensitive to the change in temperature compared to the case of  $\text{CH}_4$  capacity.

Fig. 13 shows the average enthalpy of adsorption of  $\text{CO}_2$  and  $\text{CH}_4$  weighted by the amount of adsorption for each gas in kerogen type II of different thermal maturity levels. The average enthalpy of adsorption is evaluated at different pressures for temperatures of 330 K and 400 K. Similarly, as the case of different kerogen types, we observe that  $\text{CO}_2$  has higher enthalpy of adsorption compared to  $\text{CH}_4$  for kerogen types IIA, IIB, IIC, and IID. However, for different kerogen structures with various chemical compositions and porosity, the relationship between the total adsorption capacity and the enthalpy of adsorption is not necessarily directly proportional. Although an increase in thermal maturity typically enhances the  $\text{CO}_2$  adsorption capacity, the corresponding changes in the enthalpy of adsorption do not exhibit a consistent or predictable pattern.

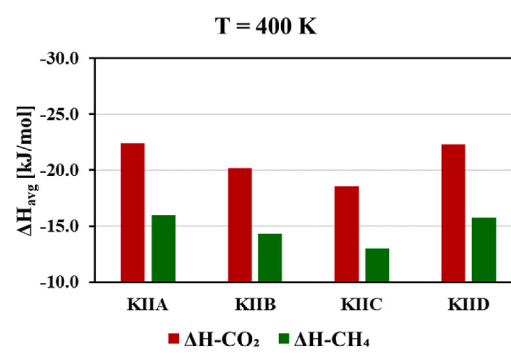
The adsorption selectivity of the  $\text{CO}_2$  over  $\text{CH}_4$  gives an indication of the surface adsorption affinity for the adsorbate gases. Selectivity values greater than 1.0 means that  $\text{CO}_2$  is adsorbed more preferentially than  $\text{CH}_4$ . Fig. 14 shows the  $\text{CO}_2$  adsorption selectivity for all the tested kerogen structures at pressures of 1, 10, and 20 MPa at 330 K. Results show that increasing the gas pressure leads to a decrease in the  $\text{CO}_2/\text{CH}_4$  selectivity. This is attributed to the increased number of molecules of each gas species at high pressure which makes the adsorption process more competitive due to the increased repulsion forces between the gas molecules. Hence, lower reservoir pressure leads to higher adsorption capacity as well as higher  $\text{CO}_2/\text{CH}_4$  selectivity. This implies the high impact of the reservoir pressure on the efficiency of the  $\text{CO}_2$  storage process in depleted shale-gas reservoirs with different kerogen types. Moreover, the type and thermal maturity of the organic matter will highly impact the methane desorption and production due to varying  $\text{CO}_2/\text{CH}_4$  selectivity associated with the different kerogen structures and hence impacting the EGR process in organic-rich gas reservoirs.

### 3.5. Impact of moisture and oil content on the $\text{CO}_2$ adsorption capacity of kerogen IID

Kerogen IID is recognized as a gas-prone kerogen, rich in organic matter capable of generating hydrocarbon gases such as methane. In shale-gas reservoirs, water is commonly present alongside other hydrocarbon fluids. Water exists in organic shale-gas reservoirs as native formation water especially in unfractured shales where pore spaces host free water, capillary-bound water in mesopores, and clay-bound water within nanopores and interlayers of clay minerals (Mu et al., 2021). Moreover, water can be introduced into these reservoirs during the hydraulic fracturing operations. Another source of water in organic shales is the thermogenic water that is produced from the cracking of the organic matter (Behar et al., 2003; Lewan and Roy, 2011). Meanwhile, as reservoir pressure declines, heavier gas molecules tend to aggregate,



(a)



(b)

Fig. 13. The adsorption-weighted average of the enthalpy of adsorption for both  $\text{CO}_2$  and  $\text{CH}_4$  for kerogen types IIA, IIB, IIC, and IID at temperatures of (a) 330 K and (b) 400 K.

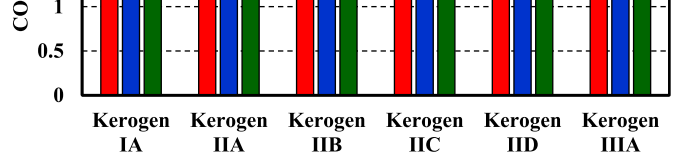


Fig. 14. The  $\text{CO}_2/\text{CH}_4$  selectivity for the different kerogen structures at 330 K and pressures of 1, 10, and 20 MPa.

forming a condensate (light oil) phase. To evaluate the impact of oil and water on the  $\text{CO}_2$  adsorption capacity of shale-gas reservoirs, we developed several scenarios with varying water and oil contents (0 wt%, 1 wt%, 2 wt%, and 3 wt%) within the kerogen IID structure at 330 K. The  $\text{CO}_2$  adsorption isotherms for kerogen IID in the presence of oil and water were reported by Gomaa et al. (2023b).

Fig. 15 illustrates the relative percentage reduction in adsorption isotherms for saturated kerogen IID compared to dry conditions. The

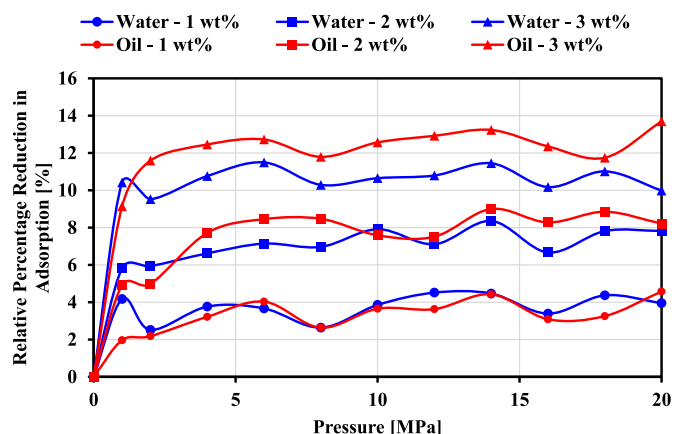


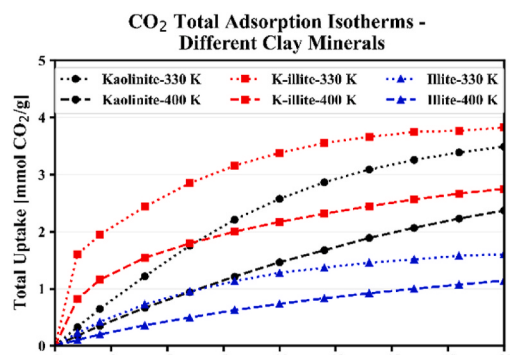
Fig. 15. The relative percentage reduction in  $\text{CO}_2$  adsorption in kerogen IID with different concentrations of moisture and oil content, evaluated at a temperature of 330 K and a pressure range of 0–20 MPa.

addition of water or oil to the kerogen structure results in a decrease in  $\text{CO}_2$  adsorption capacity. This reduction can be attributed to a decrease in available pore volume and fewer adsorption sites for  $\text{CO}_2$ . The maximum adsorption capacity of kerogen IID is reduced by 10 % and 13.7 % in the cases of 3 wt% water and oil saturations, respectively. At low fluid saturations (e.g., 1 wt%), the reductions in  $\text{CO}_2$  adsorption capacity are nearly identical for both water and oil. However, as saturation levels increase, the impact of oil becomes more pronounced than that of water. This difference is likely due to the larger size of decane molecules, representing the oil content, compared to water molecules.

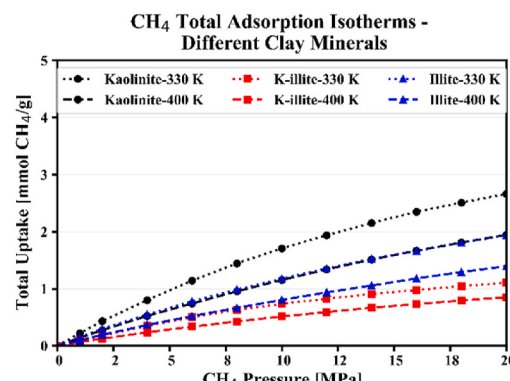
### 3.6. Impact of Clay Surface Charge on the $\text{CO}_2:\text{CH}_4$ competitive adsorption

The surface charge of clay minerals plays a crucial role in the competitive adsorption of  $\text{CO}_2$  and  $\text{CH}_4$ . To quantify this effect, we developed clay minerals with varying surface charges. In this study, the kaolinite structure is designed to be neutrally charged, the illite structure is given a negative charge, and the K-illite structure is modified to carry a partial positive charge due to potassium ions attached to its surface. All clay structures share a consistent pore size of 2 nm. Fig. 16 presents the competitive adsorption isotherms for both  $\text{CO}_2$  and  $\text{CH}_4$ , evaluated at temperatures of 330 K and 400 K across a pressure range of 0–20 MPa for the three clay structures. The results reveal that the K-illite structure, with its partial positive charge, exhibits the highest  $\text{CO}_2$  adsorption capacity among the clay minerals. This is attributed to the strong attractive forces between  $\text{CO}_2$  molecules and the positively charged potassium ions. Conversely, the negatively charged illite structure shows a reduced  $\text{CO}_2$  adsorption capacity due to the repulsion between  $\text{CO}_2$  molecules and the clay surface. Meanwhile, neutral kaolinite demonstrates a moderate  $\text{CO}_2$  adsorption capacity, falling between those of K-illite and illite.

In contrast, K-illite exhibits the lowest affinity for  $\text{CH}_4$  compared to the illite and kaolinite structures. This results in a high  $\text{CO}_2/\text{CH}_4$  selectivity for K-illite, reaching up to 17.2 at 330 K and 1 MPa, as shown in Fig. 17. The figure also illustrates the significant influence of clay surface chemistry, pressure, and temperature on  $\text{CO}_2/\text{CH}_4$  selectivity. Kaolinite maintains a relatively constant  $\text{CO}_2/\text{CH}_4$  selectivity of just below 1.5 across the tested pressures and temperatures. On the other hand, negatively charged illite demonstrates a  $\text{CO}_2/\text{CH}_4$  selectivity of less than 1, indicating a lower affinity for  $\text{CO}_2$  compared to methane. This behavior is likely due to strong repulsive forces between the  $\text{CO}_2$  molecules and the negatively charged clay surface. Additionally, the results underscore the inverse relationship between system pressure and temperature and  $\text{CO}_2/\text{CH}_4$  selectivity, with pressure having a more pronounced effect on gas selectivity than temperature. These selectivity



(a)



(b)

Fig. 16. The (a)  $\text{CO}_2$  and (b)  $\text{CH}_4$  competitive adsorption isotherms of clay minerals, kaolinite, illite, and K-illite at temperatures of 330 K and 400 K, evaluated at a pressure range of 0–20 MPa.

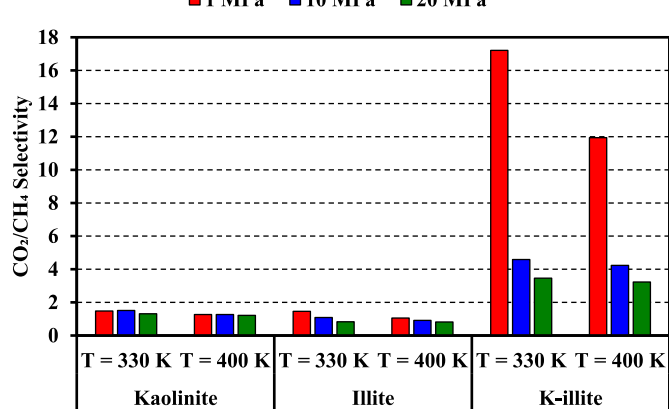


Fig. 17. The adsorption selectivity of  $\text{CO}_2/\text{CH}_4$  for Kaolinite, Illite, and K-illite clay structures at temperatures of 400 K, evaluated at a pressure range of 1–20 MPa.

results can also be used as a valuable input for EGR criteria in clay-rich depleted gas reservoirs.

To quantitatively evaluate the amount of gas trapped within the clay nanopores through adsorption at 20 MPa, we analyzed the molecular number density profiles of  $\text{CO}_2$  and  $\text{CH}_4$  across the pore channels of different clay structures. Fig. 18 presents the number density distributions of both gases along the Z-axis direction within the nanopores. In the case of illite and K-illite structures, a clearly defined adsorption layer of approximately 5 Å thickness is observed. In comparison, the adsorption layer in the kaolinite structure is present, but less pronounced compared to the other two clay minerals. These findings indicate that illite surfaces, particularly those with potassium ( $\text{K}^+$ ) cations, exhibit higher adsorption selectivity towards  $\text{CO}_2$ . The enhanced selectivity in K-illite is likely due to electrostatic interactions facilitated by the positively charged potassium ions present at the clay surface.

### 3.7. Impact of moisture and oil content on the $\text{CO}_2$ adsorption capacity of clay structures

Moisture and oil content of clay structures can reduce their  $\text{CO}_2$  storage capacity by occupying part of the pore space available for adsorption as well as changing the distribution of the electrostatic charges in the pore space. We simulated the adsorption process for  $\text{CO}_2$  gas in both K-illite and kaolinite clay structures under different cases of moisture and oil content. The  $\text{CO}_2$  adsorption isotherms for the clay minerals in the presence of oil and water were reported by Gomaa et al.

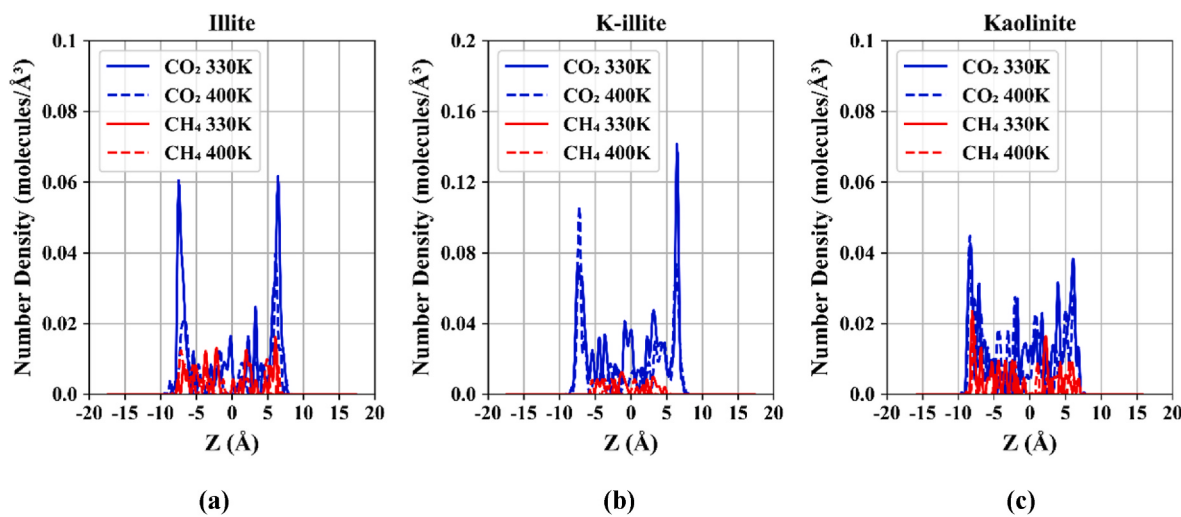


**Fig. 18.** The molecular number density of both CO<sub>2</sub> and CH<sub>4</sub> evaluated at 20 MPa at temperatures of 330 K and 400 K within (a) illite, (b) K-illite, and (c) kaolinite clay structures.

(2023b). Fig. 19 demonstrates the relative percentage reduction in CO<sub>2</sub> adsorption isotherms for the saturated K-illite compared to the dry structure. We notice that at pressures lower than 5 MPa, adding polar water molecules to the illite structure in the presence of positive potassium cations leads to a decrease in the CO<sub>2</sub> adsorption capacity as water adheres more to the clay surface than CO<sub>2</sub>. On the other hand, introducing decane to the K-illite pores slightly increases CO<sub>2</sub> adsorption at low pressures. This is attributed to the favorable electrostatic interactions between CO<sub>2</sub> and decane molecules. The primary interaction between CO<sub>2</sub> and decane molecules is through van der Waals forces. These forces arise due to temporary fluctuations in electron density within the molecules, leading to induced dipoles that attract each other. However, at higher pressures (i.e., higher than 5 MPa), the CO<sub>2</sub> adsorption process is more governed by the available unoccupied pore space than the electrostatic interactions by the molecular species in the system. That is why there is a reduction in CO<sub>2</sub> adsorption at higher pressures in the presence of both oil and water molecules.

Fig. 20 illustrates the relative percentage reduction in CO<sub>2</sub> adsorption isotherms for saturated kaolinite compared to the dry structure. Contrary to the previous observations with K-illite, the introduction of both water and decane molecules into kaolinite pores leads to an increase in CO<sub>2</sub> adsorption capacity at low pressures. In the water-saturated cases, this increase is attributed to the electrostatic

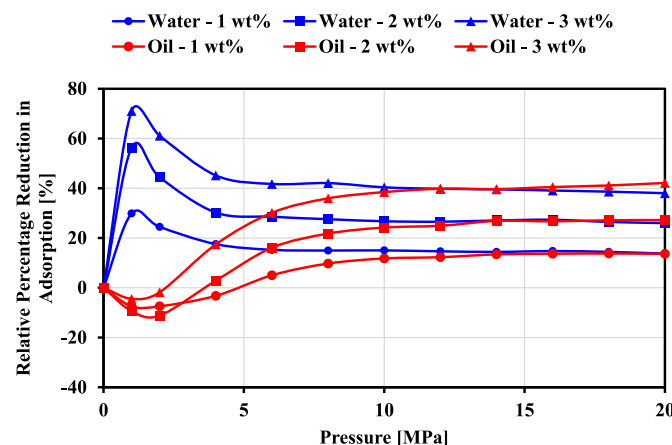


**Fig. 19.** The relative percentage reduction in CO<sub>2</sub> adsorption in K-illite with different concentrations of moisture and oil content, evaluated at a temperature of 330 K and a pressure range of 0–20 MPa.

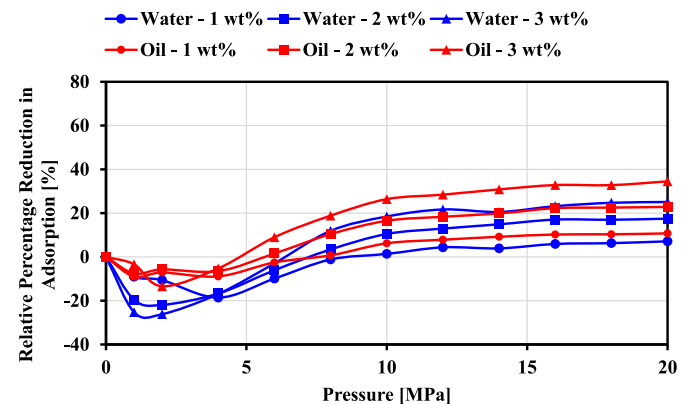


**Fig. 20.** The relative percentage reduction in CO<sub>2</sub> adsorption in kaolinite with different concentrations of moisture and oil content, evaluated at a temperature of 330 K and a pressure range of 0–20 MPa.

attractions between the polar water molecules and CO<sub>2</sub>, which enhances CO<sub>2</sub> adsorption in the neutral kaolinite pores. Similarly, but to a lesser extent, weaker attractive forces between decane molecules and CO<sub>2</sub> contribute to the increased CO<sub>2</sub> adsorption in decane-saturated kaolinite at low pressures.

As the pressure exceeds 5 MPa, the governing mechanism for CO<sub>2</sub> adsorption shifts from being driven by electrostatic interactions between CO<sub>2</sub> and the rock and fluid components to being more influenced by the availability of adsorption sites for CO<sub>2</sub>. Consequently, there is a reduction in CO<sub>2</sub> adsorption for both water and oil-saturated cases at higher pressures, with the extent of reduction correlating with the level of saturation—the higher the saturation, the greater the reduction in CO<sub>2</sub> adsorption capacity. Notably, the reduction is more pronounced in oil-saturated cases than in water-saturated ones, even at equivalent saturation levels. This is due to the larger size of decane molecules compared to water molecules, which causes decane to occupy more adsorption sites, thereby inhibiting CO<sub>2</sub> adsorption more than water. Busch et al. (2008) investigated the impact of moisture content on the CO<sub>2</sub> adsorption capacity of montmorillonite, illite, and kaolinite clay samples. Unlike other clay minerals, kaolinite clay with 0.1 % water content experienced an increase in the adsorption capacity compared to the dry sample. Meanwhile, illite sample with 2.4 % water content showed a sharp reduction in CO<sub>2</sub> adsorption at low pressures compared to higher pressures. These results validate the results shown in Figs. 14 and 15.

regarding the impact of water content on the CO<sub>2</sub> adsorption capacity of the tested clay minerals.

### 3.8. Comparison between MD simulations and experimental results

The simulation results about the impacts of temperature, fluid content, kerogen type, and kerogen thermal maturity on gas adsorption align quantitatively and qualitatively with the previously documented experimental findings by Ross and Bustin (2007), Ross and Bustin (2009), Chalmers and Bustin (2008), Zhang et al. (2012), Haiyan (2014), Heller and Zoback (2014), Rexer et al. (2014), Cancino et al. (2017), Zou et al. (2019), Ansari et al. (2022), Zhang et al. (2022), and Murugesu et al. (2023) regarding gas adsorption in organic-rich shale formations. Similarly, experimental observations by Busch et al. (2008), Heller and Zoback (2014), Du et al. (2022), and Grekov et al. (2023) on the influence of moisture and temperature on methane adsorption in clay samples are in agreement with the MD simulation results of clay models documented in this paper. For instance, Grekov et al. (2023) showed a reduction of about 80 % in the CO<sub>2</sub> adsorption capacity of illite clay after being fully saturated with water. Meanwhile, Ross and Bustin (2007) evaluated the methane adsorption capacity for both dry and 8.5 wt% water-saturated organic-rich shale sample. They reported a stable 25 % reduction in the methane adsorption capacity at pressures higher than 4 MPa due to the presence of water. These observations are consistent with the CO<sub>2</sub> adsorption behavior observed in our modeled clay and kerogen structures across varying moisture levels.

For the purpose of direct quantitative verification of MD modeling, the results should be compared with adsorption experimental data performed with pure rock components such as kerogen and clay samples under the same pressure, temperature, and pore structure as those of the MD models. Therefore, we compared the methane adsorption capacities of different kerogen types and different thermal maturity levels against experimental data reported by Zhang et al. (2012), Haiyan (2014), and Rexer et al. (2014). In their study, Zhang et al. (2012) extracted pure kerogen samples from Green River shale, Woodford shale, and Cameo coal, representing kerogen Types I, II, and III, respectively. Methane adsorption on these samples was then evaluated using the manometric gas adsorption technique at temperatures of 308.15, 323.15, and 338.15 K, with pressures up to 15 MPa. Haiyan (2014) isolated kerogen type II samples from Barnett shale and divided them into immature and mature samples. He then measured the CH<sub>4</sub> adsorption isotherms under four different temperatures (i.e., 308.15 K, 323.215 K, 338.15 K, and 348.15 K) for the pressure range 0–13 MPa. Meanwhile, Rexer et al. (2014) evaluated the methane adsorption isotherms of three different kerogen type II samples extracted from Posidonia shales. They divided the kerogen samples into low thermal maturity samples (i.e., WIC7145 and WIC7155), thermally mature samples (i.e., HAR7038 and HAR7060), and over-mature samples (i.e., HAD7090 and HAD7119). They then evaluated the methane adsorption on the kerogen samples at two different temperatures of 318.15 K and 338.15 K for pressures up to 16 MPa.

The aforementioned experimental studies align closely with those

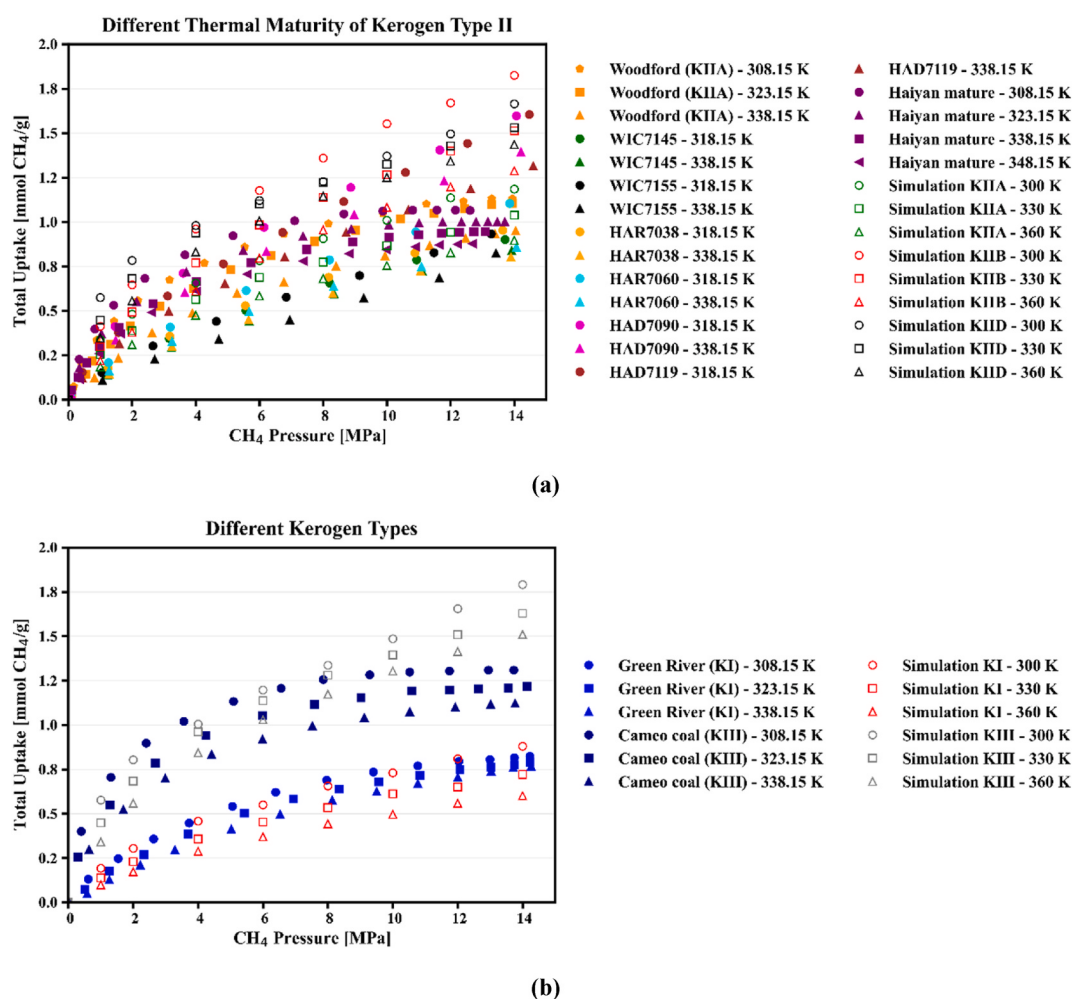


Fig. 21. Comparison between the methane adsorption isotherms obtained from the MD simulations in this paper and the experimental results reported by Zhang et al. (2012), Haiyan (2014), and Rexer et al. (2014) for (a) Kerogen Type II, (b) Kerogen Types II and III.

adopted in our MD simulations, providing a robust basis for comparison. Fig. 21a illustrates the experimental results for methane adsorption on kerogen type II of different thermal maturity levels alongside our simulation results under similar pressure and temperature conditions. The order of methane adsorption capacity observed in the experimental samples—Kerogen Type IID > Kerogen Type IIB > Kerogen Type IIA—mirrors the trends observed in the simulation results. For the other types of kerogen structures, Fig. 21b shows a comparison between the samples reported in Zhang et al. (2012) and the results of MD simulations. The methane adsorption isotherms from the MD simulations closely match the experimental values, though some deviations arise due to differences in temperatures and the scale of investigation. This agreement between the simulation and experimental investigations lends additional credibility to the findings from molecular-scale simulations documented in this paper.

### 3.9. Suggestions for possible field applications of the findings

The quantification of the CO<sub>2</sub> total adsorption capacity as well as the CO<sub>2</sub>/CH<sub>4</sub> of the solid components of organic shale formations enables choosing the best candidate reservoir for EGR and CO<sub>2</sub> storage. Moreover, the investigation of the impact of moisture and oil content on CO<sub>2</sub> adsorption can help us predict the amount of CO<sub>2</sub> that will be trapped by either dissolution or adsorption trapping. Moreover, the total CO<sub>2</sub> storage capacity of organic shale will highly depend on the amount of adsorbed gas phase. For instance, Bachu et al. (2007) suggested calculating the CO<sub>2</sub> storage capacity of coal beds by analogy with the gas reserves estimation methods in such reservoirs via

$$M_{CO_2} = Ah(1 - f_a - f_m)\rho_{CO_2}n_cG_c, \quad (6)$$

where  $M_{CO_2}$  is the mass of CO<sub>2</sub>,  $A$  is the reservoir area,  $h$  is the thickness,  $f_a$ , and  $f_m$  are the ash and moisture weight fraction of coal,  $\rho_{CO_2}$  is the density of CO<sub>2</sub>,  $n_c$  is the bulk coal density, and  $G_c$  is the gas coal content that can be calculated by

$$G_c = V_L \frac{P}{P + P_L}, \quad (7)$$

where  $V_L$  and  $P_L$  are the Langmuir volume and pressure, respectively, and  $P$  is the gas pressure.

Moreover, Ambrose et al. (2012) proposed a model to calculate the free gas in-place in organic-rich mudrocks in which he accounted for the volume of the adsorbed gas phase as

$$G_f = \frac{\phi(1 - S_w) - \phi_a}{\rho_b B_g}, \quad (8)$$

where  $G_f$  is the free-gas storage capacity,  $\phi$  is the total porosity fraction,  $S_w$  is the water saturation,  $\phi_a$  is the sorbed-phase porosity fraction,  $\rho_b$  is the bulk-rock density, and  $B_g$  is the gas formation volume factor, reservoir volume/surface volume. The sorbed-phase porosity depends highly on the volume and density of sorbed gas and can be calculated by

$$\phi_a = M \frac{\rho_b}{\rho_s} \left( V_L \frac{P}{P + P_L} \right), \quad (9)$$

where  $M$  is the apparent natural gas molecular weight, and  $\rho_s$  is the sorbed-phase density.

From the discussed models, one can see how the accurate calculations of the CO<sub>2</sub> storage in organic-rich mudrocks need an accurate quantification of the adsorption isotherms under various reservoir conditions, which can be directly obtained from the proposed molecular-scale modeling.

## 4. Conclusions

In this study, we explored the various factors influencing CO<sub>2</sub>

competitive adsorption within two key components of shale-gas reservoirs: kerogen and clay minerals. Using molecular models of different kerogen and clay types with varying thermal maturity levels and surface charges, we conducted Grand Canonical Monte Carlo (GCMC) adsorption simulations at pressures up to 20 MPa and temperatures of 330 K and 400 K. Additionally, we assessed CO<sub>2</sub>/CH<sub>4</sub> adsorption selectivity to identify the optimal organic shale composition for CO<sub>2</sub> storage applications. The key findings of this research are as follows.

- **Kerogen Type Influence:** Transitioning from kerogen type IA to IIIA resulted in a fourfold increase in maximum CO<sub>2</sub> adsorption capacity at 330 K. Moreover, kerogen type IIIA exhibited a significantly higher CO<sub>2</sub>/CH<sub>4</sub> adsorption selectivity—92 % greater than type IA and 42 % greater than type IIA. This underscores the profound impact of kerogen type on the anticipated CO<sub>2</sub> storage capacity in the presence of methane.
- **Effect of Kerogen Thermal Maturity:** Increasing the thermal maturity of kerogen from type IIA to IID induced various compositional and structural changes, leading to a greater number of available adsorption sites within the kerogen matrix. Consequently, the CO<sub>2</sub> adsorption capacity of type IID was double that of type IIA. Although types IIB and IIC also showed higher adsorption capacities compared to type IIA, type IIA demonstrated superior CO<sub>2</sub>/CH<sub>4</sub> adsorption selectivity—28 % and 34 % higher than types IIB and IIC, respectively, at 330 K and 20 MPa. This highlights the necessity of evaluating CO<sub>2</sub>/CH<sub>4</sub> selectivity before conducting CO<sub>2</sub> storage operations in shale-gas reservoirs.
- **Impact of Clay Surface Charge:** The surface charge of clay minerals greatly influenced both adsorption capacity and CO<sub>2</sub>/CH<sub>4</sub> selectivity. Introducing positive potassium ions to the K-illite clay surface increased its CO<sub>2</sub> adsorption capacity by 133 % compared to negatively charged illite clay. Neutral kaolinite showed intermediate behavior between K-illite and illite, further emphasizing the role of surface charge in adsorption performance.
- **Effect of Reservoir Moisture and Oil Content:** The presence of moisture and oil in the reservoir significantly reduced the CO<sub>2</sub> adsorption capacity of both kerogen and clay structures, with reductions ranging from 4 % to 42 % at 3 wt% moisture and oil content. This finding underscores the importance of accounting for water and oil saturations when evaluating CO<sub>2</sub> storage capacity in shale-gas reservoirs.
- **Influence of Reservoir Pressure and Temperature:** Both pressure and temperature were found to critically affect CO<sub>2</sub> adsorption capacity and CO<sub>2</sub>/CH<sub>4</sub> selectivity in kerogen and clay structures. Elevated gas pressures enhanced adsorption capacity due to the microporous nature of the tested models. However, increased pressure also led to a reduction in CO<sub>2</sub>/CH<sub>4</sub> selectivity. Additionally, higher temperatures were unfavorable for CO<sub>2</sub> storage due to the exothermic nature of the adsorption process. Therefore, optimizing reservoir pressure and temperature conditions is crucial for enhancing the efficiency of EGR processes and maximizing both CO<sub>2</sub> storage capacity and CO<sub>2</sub>/CH<sub>4</sub> selectivity.
- **Validating the Simulation Results:** Gas adsorption on kerogen molecular structures—across varying types and thermal maturity levels—was rigorously compared to experimental data obtained under similar pressures and temperatures, confirming a high degree of consistency. Furthermore, the influence of moisture content on the adsorption capacity of clay minerals demonstrated good agreement with laboratory findings from corresponding clay samples. These robust correlations validate the simulation results across a wide range of sensitivity scenarios.

## CRediT authorship contribution statement

**Ibrahim Gomaa:** Writing – original draft, Visualization, Validation, Methodology, Investigation, Formal analysis, Data curation,

**Conceptualization.** Isa Silveira de Araujo: Writing – review & editing, Methodology, Investigation, Formal analysis. Zoya Heidari: Writing – review & editing, Validation, Supervision, Methodology, Investigation, Funding acquisition, Conceptualization. D. Nicolas Espinoza: Writing – review & editing, Validation, Investigation, Conceptualization.

### Declaration of competing interest

The authors declare that they have no known competing financial interests or personal relationships that could have appeared to influence the work reported in this paper.

### ACRONYMS

CEC	=	Cation Exchange Capacity
EGR	=	Enhanced Gas Recovery
GCMC	=	Grand Canonical Monte Carlo
LAMMPS	=	Large-scale Atomic/Molecular Massively Parallel Simulator
LJ	=	Lennard-Jones
OPLS-UA	=	Optimized Potential for Liquid Simulations United-Atom
TIP3P	=	Transferable Intermolecular Potential with 3 Points
TraPPE	=	Transferable Potentials for Phase Equilibria
XPS	=	X-ray Photoelectron Spectroscopy

### NOMENCLATURE

$A$	=	Reservoir area
$B_g$	=	Gas formation volume factor
$f_a$	=	Ash weight fraction
$f_m$	=	Moisture weight fraction
$G_c$	=	Gas coal content
$G_f$	=	Free-gas storage capacity
$h$	=	Reservoir thickness
$M$	=	Apparent natural gas molecular weight
$M_{CO_2}$	=	Mass of $CO_2$
$n_c$	=	Bulk coal density
$P$	=	Gas pressure
$P_L$	=	Langmuir pressure
$q_i$	=	Atomic charge of atoms $i$ , e
$Q_i$	=	The amount of gas adsorbed at pressure $i$
$q_j$	=	Atomic charge of atoms $j$ , e
$r_{ij}$	=	Distance between atoms $i$ and $j$ , Å
$S_w$	=	Water saturation
$U$	=	Total nonbonded intermolecular potential, kcal/mol
$V_L$	=	Langmuir volume
$x_{CH_4}$	=	The average mole fraction of $CH_4$ in the adsorbed phase
$x_{CO_2}$	=	The average mole fraction of $CO_2$ in the adsorbed phase
$y_{CO_2}$	=	The average mole fraction of $CO_2$ in the bulk phase
$y_{CH_4}$	=	The average mole fraction of $CH_4$ in the bulk phase
$\Delta H_{avg}$	=	Adsorption-weighted average for the enthalpy of adsorption
$\Delta H_i$	=	Enthalpy of adsorption of gas species at pressure $i$
$\epsilon_0$	=	Electric constant
$\epsilon_{ij}$	=	Depth of the potential well (dispersion energy), kcal/mol
$\rho_b$	=	Bulk-rock density
$\rho_{CO_2}$	=	Density of $CO_2$
$\rho_s$	=	Sorbed-phase density
$\sigma_{ij}$	=	Collision diameter (size of the particle), Å
$\phi$	=	Total porosity fraction
$\phi_a$	=	Sorbed-phase porosity fraction

### Data availability

Data will be made available on request.

### Acknowledgments

The authors acknowledge the industry members of the University of Texas at Austin's Industrial Affiliates Research Program on "Multi-Scale Rock Physics" sponsored by Core Laboratories, ExxonMobil, Hilcorp, Occidental Petroleum, Pan American Energy, Petrobras, and Woodside Energy for supporting this research. The authors also acknowledge the NSF award 1834345 as well as the Texas Advanced Computing Center (TACC) at The University of Texas at Austin for providing high-performance computing resources that have contributed to the research results reported within this paper.

### References

- Abdalla, M.A.M., Peng, H., Wu, D., et al., 2018. Prediction of hydrophobic reagent for flotation process using molecular modeling. ACS Omega 3, 6483–6496. [https://doi.org/10.1021/ACSOMEA.8B00413/SUPPL\\_FILE/AO8B00413\\_SI\\_001.PDF](https://doi.org/10.1021/ACSOMEA.8B00413/SUPPL_FILE/AO8B00413_SI_001.PDF).
- Alafnan, S., Soling, T., Mahmoud, M., 2020. Effect of kerogen thermal maturity on methane adsorption capacity: a molecular modeling approach. Molecules 25 (16), 3764. <https://doi.org/10.3390/molecules25163764>.

- Ambrose, R.J., Hartman, R.C., Diaz-Campos, M., et al., 2012. Shale gas-in-place calculations Part I: new pore-scale considerations. *SPE Journal* 17, 219–229. <https://doi.org/10.2118/131772-PA>.
- Ansari, H., Gong, S., Trusler, J.M., et al., 2022. Hybrid pore-scale adsorption model for CO<sub>2</sub> and CH<sub>4</sub> storage in shale. *Energy Fuels* 36 (7), 3443–3456. <https://doi.org/10.1021/acs.energyfuels.1c03723>.
- Araujo, I.S., Heidari, Z., 2022. Quantification of adsorption of water on clay surfaces and electrical double layer properties using molecular simulations. In: Paper SPWLA-2022-0005 presented at the SPWLA 63rd Annual Logging Symposium. <https://doi.org/10.30632/SPWLA-2022-0005>. Stavanger, Norway, June 10–15.
- Araujo, I.S., Jagadisian, A., Heidari, Z., 2023. Impacts of kerogen type and thermal maturity on methane and water adsorption isotherms: A molecular simulation approach. *Fuel* 352, 128944. <https://doi.org/10.1016/J.FUEL.2023.128944>.
- Bachu, S., Bonijoly, D., Bradshaw, J., et al., 2007. CO<sub>2</sub> storage capacity estimation: Methodology and gaps. *Int. J. Greenh. Gas Control* 1, 430–443. [https://doi.org/10.1016/S1750-5836\(07\)00086-2](https://doi.org/10.1016/S1750-5836(07)00086-2).
- Behar, F., Lewan, M.D., Lorant, F., Vandembroucke, M., 2003. Comparison of artificial maturation of lignite in hydrous and nonhydrous conditions. *Org. Geochem.* 34, 575–600. [https://doi.org/10.1016/S0146-6380\(02\)00241-3](https://doi.org/10.1016/S0146-6380(02)00241-3).
- Bish, D.L., 1993. Rietveld refinement of the kaolinite structure at 1.5 K. *Clays Clay Miner.* 41, 738–744. <https://doi.org/10.1346/CCMN.1993.0410613/METRICS>.
- Bondi, A., 1964. Van der waals volumes and radii. *J. Phys. Chem.* 68, 441–451. [https://doi.org/10.1021/J100785A001/ASSET/J100785A001.FP.PNG\\_V03](https://doi.org/10.1021/J100785A001/ASSET/J100785A001.FP.PNG_V03).
- Bonnaud, P.A., Oulebsir, F., Galliero, G., et al., 2023. Modeling competitive adsorption and diffusion of CH<sub>4</sub>/CO<sub>2</sub> mixtures confined in mature type-II kerogen: insights from molecular dynamics simulations. *Fuel* 352. <https://doi.org/10.1016/j.fuel.2023.129020>.
- Busch, A., Alles, S., Gensterblum, Y., et al., 2008. Carbon dioxide storage potential of shales. *Int. J. Greenh. Gas Control* 2, 297–308. <https://doi.org/10.1016/J.IJGGC.2008.03.003>.
- Busch, A., Bertier, P., Gensterblum, Y., et al., 2016. On sorption and swelling of CO<sub>2</sub> in clays. *Geomechanics and Geophysics for Geo-Energy and Geo-Resources* 2, 111–130. <https://doi.org/10.1007/S40948-016-0024-4/FIGURES/8>.
- Cancino, O.P.O., Pérez, D.P., Pozo, M., et al., 2017. Adsorption of pure CO<sub>2</sub> and a CO<sub>2</sub>/CH<sub>4</sub> mixture on a black shale sample: manometry and microcalorimetry measurements. *J. Petrol. Sci. Eng.* 159, 307–313. <https://doi.org/10.1016/j.petrol.2017.09.038>.
- Chalmers, G.R., Bustin, R.M., 2008. Lower Cretaceous gas shales in northeastern British Columbia, Part I: geological controls on methane sorption capacity. *Bull. Can. Petrol. Geol.* 56 (1), 1–21. <https://doi.org/10.2113/gscgbull.56.1.1>.
- Chen, Y.H., Lu, D.L., 2015. CO<sub>2</sub> capture by kaolinite and its adsorption mechanism. *Appl. Clay Sci.* 104, 221–228. <https://doi.org/10.1016/J.CLAY.2014.11.036>.
- Cygan, R.T., Liang, J., Kalinichev, A.G., 2004. Molecular models of hydroxide, oxyhydroxide, and clay phases and the development of a general force field. *J. Phys. Chem. B* 108 (4), 1255–1266. <https://doi.org/10.1021/jp0363287>.
- Dang, S.T., Sondergeld, C.H., Rai, C.S., 2016. A new approach to measure organic density. *Petrophysics* 57 (2), 112–120. <https://doi.org/10.15530/URTEC-2014-1921752>.
- Dauber-Osguthorpe, P., Roberts, V.A., Osguthorpe, D.J., et al., 1988. Structure and energetics of ligand binding to proteins: *Escherichia coli* dihydrofolate reductase-trimethoprim, a drug-receptor system. *Proteins: Struct., Funct., Bioinf.* 4, 31–47. <https://doi.org/10.1002/prot.340040106>.
- Du, F., Nojabaei, B., 2019. A review of gas injection in shale reservoirs: enhanced Oil/Gas recovery approaches and greenhouse gas control. *Energies* 12 (12), 2355. <https://doi.org/10.3390/en12122355>.
- Du, X., Pang, D., Zhao, Y., et al., 2022. Investigation into the adsorption of CO<sub>2</sub>, N<sub>2</sub> and CH<sub>4</sub> on kaolinite clay. *Arab. J. Chem.* 15. <https://doi.org/10.1016/j.arabjc.2021.103665>.
- Dubbeldam, D., Calero, S., Ellis, D.E., et al., 2016. RASPAs: molecular simulation software for adsorption and diffusion in flexible nanoporous materials. *Mol. Simul.* 42, 81–101. <https://doi.org/10.1080/08927022.2015.1010082>.
- Duncan, D.C., Swanson, V.E., 1966. *Organic-Rich Shale of the United States and World Land Areas*, vol.523. *Geological Survey Circular*.
- Ekundayo, J.M., Rezaee, R., Fan, C., 2021. Experimental investigation and mathematical modelling of shale gas adsorption and desorption hysteresis. *J. Nat. Gas Sci. Eng.* 88, 103761. <https://doi.org/10.1016/J.JNGSE.2020.103761>.
- Forsman, J.P., Hunt, J.M., 1958. Insoluble organic matter (kerogen) in sedimentary rocks. *Geochim. Cosmochim. Acta* 15 (3), 170–182. [https://doi.org/10.1016/0016-7037\(58\)90055-3](https://doi.org/10.1016/0016-7037(58)90055-3).
- Frost, L.R., Kristof, J., 2004. Raman and infrared spectroscopic studies of kaolinite surfaces modified by intercalation. In: Wypych, F., Satyanarayana, K.G. (Eds.), *Clay Surfaces: Fundamentals and Applications*. Elsevier, London. [https://doi.org/10.1016/S1573-4285\(04\)80041-3](https://doi.org/10.1016/S1573-4285(04)80041-3).
- Gelb, L.D., Gubbins, K.E., 1999. Pore size distributions in porous glasses: a computer simulation study. *Langmuir* 15 (2), 305–308. <https://doi.org/10.1021/la9808418>.
- Gomaa, I., Araujo, I.S., Heidari, Z., Espinoza, D.N., 2023b. Molecular simulation study of the competitive adsorption of carbon dioxide and methane in organic shale – implication for enhanced gas recovery. In: Paper URTEC-3858281-MS Presented at the SPE/AAPG/SEG Unconventional Resources Technology Conference. Denver, Colorado, USA. June 13–15.
- Gomaa, I., Guerrero, J., Heidari, Z., et al., 2023a. Experimental measurements and molecular simulation of carbon dioxide adsorption on carbon surface. *SPE Res Eval & Eng* 1–14. <https://doi.org/10.2118/210264-PA>. SPE-210264-PA.
- Gomaa, I., Heidari, Z., Espinoza, D.N., 2023c. Molecular-scale quantitative evaluation of the competitive sorption of methane and carbon dioxide on the different constituents of organic-rich mudrocks. In: Paper SPWLA-2023-1826 Presented at the SPWLA 64th Annual Logging Symposium. Stavanger, Lake Conroe, Texas, USA. June 10–14.
- Grekov, D.I., Robinet, J., Grambow, B., 2023. Adsorption of methane and carbon dioxide by water-saturated clay minerals and clay rocks. *Appl. Clay Sci.* 232, 106806. <https://doi.org/10.1016/j.clay.2022.106806>.
- Haiyan, H., 2014. Methane adsorption comparison of different thermal maturity kerogens in shale gas system. *Chin. J. Geochem.* 33, 425–430. <https://doi.org/10.1007/S11631-014-0708-9/METRICS>.
- Hamza, A., Hussein, I.A., Al-Marri, M.J., et al., 2021. Impact of clays on CO<sub>2</sub> adsorption and enhanced gas recovery in sandstone reservoirs. *Int. J. Greenh. Gas Control* 106, 103286. <https://doi.org/10.1016/J.IJGGC.2021.103286>.
- Heinz, H., Vaia, R.A., Farmer, B.L., et al., 2008. Accurate simulation of surfaces and interfaces of face-centered cubic metals using 12-6 and 9-6 Lennard-Jones potentials. *J. Phys. Chem. C* 112, 17281–17290. <https://doi.org/10.1021/jp801931d>.
- Heller, R., Zoback, M., 2014. Adsorption of methane and carbon dioxide on gas shale and pure mineral samples. *Journal of Unconventional Oil and Gas Resources* 8, 14–24. <https://doi.org/10.1016/j.juogr.2014.06.001>.
- Hu, X., Deng, H., Lu, C., et al., 2019. Characterization of CO<sub>2</sub>/CH<sub>4</sub> competitive adsorption in various clay minerals in relation to shale gas recovery from molecular simulation. *Energy Fuels* 33, 8202–8214. <https://doi.org/10.1021/acs.energyfuels.9b01610>.
- Huang, L., Ning, Z., Wang, Q., et al., 2018a. Effect of organic type and moisture on CO<sub>2</sub>/CH<sub>4</sub> competitive adsorption in kerogen with implications for CO<sub>2</sub> sequestration and enhanced CH<sub>4</sub> recovery. *Appl. Energy* 210, 28–43. <https://doi.org/10.1016/J.APENERGY.2017.10.122>.
- Huang, L., Ning, Z., Wang, Q., et al., 2018b. Molecular simulation of adsorption behaviors of methane, carbon dioxide and their mixtures on kerogen: effect of kerogen maturity and moisture content. *Fuel* 211, 159–172. <https://doi.org/10.1016/J.FUEL.2017.09.060>.
- Iglauer, S., 2018. Optimum storage depths for structural CO<sub>2</sub> trapping. *Int. J. Greenh. Gas Control* 77, 82–87. <https://doi.org/10.1016/J.IJGGC.2018.07.009>.
- Jagadisian, A., Heidari, Z., 2022. Molecular dynamic simulation of the impact of thermal maturity and reservoir temperature on the contact angle and wettability of kerogen. *Fuel* 309, 122039. <https://doi.org/10.1016/J.FUEL.2021.122039>.
- Jorgensen, W.L., McDonald, N.A., 1998. Development of an all-atom force field for heterocycles. Properties of liquid pyridine and diazenes. *J. Mol. Struct.: THEOCHEM* 424, 145–155. [https://doi.org/10.1016/S0166-1280\(97\)00237-6](https://doi.org/10.1016/S0166-1280(97)00237-6).
- Kang, G., Zhang, B., Kang, T., et al., 2020. Effect of pressure and temperature on CO<sub>2</sub>/CH<sub>4</sub> competitive adsorption on kaolinite by Monte Carlo simulations. *Materials* 13 (12), 1–12. <https://doi.org/10.3390/MA13122851>.
- Kang, S.M., Fathi, E., Ambrose, R.J., et al., 2011. Carbon dioxide storage capacity of organic-rich shales. *SPE Journal* 16 (4), 842–855. <https://doi.org/10.2118/134583-PA>.
- Kelemen, S.R., Afeworki, M., Gorbaty, M.L., et al., 2007. Direct characterization of kerogen by X-ray and solid-state <sup>13</sup>C nuclear magnetic resonance methods. *Energy Fuels* 21 (3), 1548–1561. <https://doi.org/10.1021/ef060321h>.
- Lewan, M.D., Roy, S., 2011. Role of water in hydrocarbon generation from Type-I kerogen in Mahogany oil shale of the Green River Formation. *Org. Geochem.* 42 (1), 31–41. <https://doi.org/10.1016/j.orggeochem.2010.10.004>.
- Li, W., Stevens, L.A., Zhang, B., et al., 2023. Combining molecular simulation and experiment to understand the effect of moisture on methane adsorption in kerogens. *Chemical Engineering Journal* 454, 139942. <https://doi.org/10.1016/J.CEJ.2022.139942>.
- Liu, J., Xie, L., Elsworth, D., et al., 2019. CO<sub>2</sub>/CH<sub>4</sub> competitive adsorption in shale: implications for enhancement in gas production and reduction in carbon emissions. *Environ. Sci. Technol.* 53, 9328–9336. [https://doi.org/10.1021/ACS.EST.9B02432\\_SUPPL\\_FILE/ES9B02432\\_SI\\_001.PDF](https://doi.org/10.1021/ACS.EST.9B02432_SUPPL_FILE/ES9B02432_SI_001.PDF).
- Liu, Y., Hou, J., 2020. Selective adsorption of CO<sub>2</sub>/CH<sub>4</sub> mixture on clay-rich shale using molecular simulations. *J. CO<sub>2</sub> Util.* 39, 101143. <https://doi.org/10.1016/J.JCOU.2020.02.013>.
- Mohaghheghian, E., Hassanzadeh, H., Chen, Z., 2019. CO<sub>2</sub> sequestration coupled with enhanced gas recovery in shale gas reservoirs. *J. CO<sub>2</sub> Util.* 34, 646–655. <https://doi.org/10.1016/J.JCOU.2019.08.016>.
- Mu, Y., Hu, Z., Chang, J., et al., 2021. Effect of water occurrence on shale seepage ability. *J. Petrol. Sci. Eng.* 204, 108725. <https://doi.org/10.1016/j.petrol.2021.108725>.
- Murugesu, M.P., Joewondo, N., Prasad, M., 2023. Carbon storage capacity of shale formations: mineral control on CO<sub>2</sub> adsorption. *Int. J. Greenh. Gas Control* 124, <https://doi.org/10.1016/j.ijggc.2023.103833>.
- Myers, K.J., Wignall, P.B., 1987. Understanding jurassic organic-rich mudrocks. In: Leggett, J.K., Zuffa, G.G. (Eds.), *Marine Clastic Sedimentology*. Graham & Trotman, London. <https://doi.org/10.1007/978-94-009-3241-8>. Chap. 9.
- Niu, Y., Yue, C., Li, S., et al., 2018. Influencing factors and selection of CH<sub>4</sub> and CO<sub>2</sub> adsorption on silurian shale in Yibin, Sichuan Province of China. *Energy Fuels* 32 (3), 3202–3210. [https://doi.org/10.1021/ACS.ENERGYFUELS.7B03815/ASSET/IMAGES/LARGE/EF-2017-03815F\\_0010.JPG](https://doi.org/10.1021/ACS.ENERGYFUELS.7B03815/ASSET/IMAGES/LARGE/EF-2017-03815F_0010.JPG).
- Obliger, A., Ulm, F.J., Pellenq, R., 2018. Impact of nanoporosity on hydrocarbon transport in shales' organic matter. *Nano Lett.* 18, 832–837. <https://doi.org/10.1021/acs.nanolett.7b04079>.
- Peng, X., Cao, D., Zhao, J., 2009. Grand canonical Monte Carlo simulation of methane–carbon dioxide mixtures on ordered mesoporous carbon CMK-1. *Separ. Purif. Technol.* 68 (1), 50–60. <https://doi.org/10.1016/J.SEPPUR.2009.04.005>.
- Potoff, J.J., Siepmann, J.I., 2001. Vapor-Liquid Equilibria of mixtures containing alkanes, carbon dioxide, and nitrogen. *AIChE J.* 47, 1676–1682. <https://doi.org/10.1002/AIC.690470719>.

- Rexer, T.F., Mathia, E.J., Aplin, A.C., et al., 2014. High-pressure methane adsorption and characterization of pores in posidonia shales and isolated kerogens. *Energy Fuels* 28, 2886–2901. <https://doi.org/10.1021/EF402466M>.
- Ross, D.J.K., Bustin, R.M., 2007. Shale gas potential of the lower Jurassic Gordondale member, northeastern British Columbia, Canada. *Bull. Can. Petrol. Geol.* 55 (1), 51–75. <https://doi.org/10.2113/gscpgbull.55.1.51>.
- Ross, D.J.K., Bustin, R.M., 2009. The importance of shale composition and pore structure upon gas storage potential of shale gas reservoirs. *Mar. Petrol. Geol.* 26 (6), 916–927. <https://doi.org/10.1016/j.marpetgeo.2008.06.004>.
- Shrake, A., Rupley, J.A., 1973. Environment and exposure to solvent of protein atoms. Lysozyme and insulin. *J. Mol. Biol.* 79, 351–371. [https://doi.org/10.1016/0022-2836\(73\)90011-9](https://doi.org/10.1016/0022-2836(73)90011-9).
- Sirjoosinh, A., Alavi, S., Woo, T.K., 2010. Grand-canonical Monte Carlo and molecular-dynamics simulations of carbon-dioxide and carbon-monoxide adsorption in zeolitic imidazolate framework materials. *J. Phys. Chem. C* 114 (5), 2171–2178. [https://doi.org/10.1021/JP908058N SUPPL\\_FILE/JP908058N\\_SI\\_001.PDF](https://doi.org/10.1021/JP908058N SUPPL_FILE/JP908058N_SI_001.PDF).
- Siu, S.W.I., Pluhackova, K., Böckmann, R.A., 2012. Optimization of the OPLS-AA force field for long hydrocarbons. *J. Chem. Theor. Comput.* 8 (4), 1459–1470. [https://doi.org/10.1021/CT200908R SUPPL\\_FILE/CT200908R\\_SI\\_001.PDF](https://doi.org/10.1021/CT200908R SUPPL_FILE/CT200908R_SI_001.PDF).
- Soltanian, M.R., Amoie, M.A., Gershenson, N., et al., 2017. Dissolution trapping of carbon dioxide in heterogeneous aquifers. *Environ. Sci. Technol.* 51 (13), 7732–7741. [https://doi.org/10.1021/ACS.EST.7B01540/ASSET/IMAGES/LARGE/ES-2017-01540D\\_0004.jpeg](https://doi.org/10.1021/ACS.EST.7B01540/ASSET/IMAGES/LARGE/ES-2017-01540D_0004.jpeg).
- Ulmschneider, J.P., Ulmschneider, M.B., 2009. United atom lipid parameters for combination with the optimized potentials for liquid simulations all-atom force field. *J. Chem. Theor. Comput.* 5 (7), 1803–1813. [https://doi.org/10.1021/CT900086B ASSET/IMAGES/LARGE/CT-2009-00086B\\_0011.jpeg](https://doi.org/10.1021/CT900086B ASSET/IMAGES/LARGE/CT-2009-00086B_0011.jpeg).
- Ungerer, P., Collell, J., Yiannourakou, M., 2015. Molecular modeling of the volumetric and thermodynamic properties of kerogen: influence of organic type and maturity. *Energy Fuels* 29, 91–105. <https://doi.org/10.1021/ef502154k>.
- Wang, T., Tian, S., Li, G., et al., 2018. Selective adsorption of supercritical carbon dioxide and methane binary mixture in shale kerogen nanopores. *J. Nat. Gas Sci. Eng.* 50, 181–188. <https://doi.org/10.1016/J.JNGSE.2017.12.002>.
- Wang, X., Zhou, J., Sun, X., et al., 2021. The influences of composition and pore structure on the adsorption behavior of CH<sub>4</sub> and CO<sub>2</sub> on shale. *Front. Earth Sci.* 15 (2), 283–300. <https://doi.org/10.1007/S11707-021-0879-8/METRICS>.
- Widom, B., 1963. Some topics in the theory of fluids. *J. Chem. Phys.* 39, 2808–2812. <https://doi.org/10.1063/1.1734110>.
- Xie, W., Wang, M., Wang, H., 2021. Adsorption characteristics of CH<sub>4</sub> and CO<sub>2</sub> in shale at high pressure and temperature. *ACS Omega* 6 (28), 18527–18536. [https://doi.org/10.1021/ACSM/OMEGA.1C02921/ASSET/IMAGES/LARGE/AO1C02921\\_0011.jpeg](https://doi.org/10.1021/ACSM/OMEGA.1C02921/ASSET/IMAGES/LARGE/AO1C02921_0011.jpeg).
- Xiong, J., Liu, X.J., Liang, L.X., et al., 2017. Investigation of methane adsorption on chlorite by grand canonical Monte Carlo simulations. *Pet. Sci.* 14 (1), 37–49. <https://doi.org/10.1007/S12182-016-0142-1/FIGURES/18>.
- Yuan, S., Gang, H.Z., Liu, Y.F., et al., 2022. Adsorption and diffusion behaviors of CO<sub>2</sub> and CH<sub>4</sub> mixtures in different types of kerogens and their roles in enhanced energy recovery. *Sustainability (Basel)* 14. <https://doi.org/10.3390/su142214949>.
- Zhang, T., Ellis, G.S., Ruppel, S.C., et al., 2012. Effect of organic-matter type and thermal maturity on methane adsorption in shale-gas systems. *Org. Geochem.* 47, 120–131. <https://doi.org/10.1016/J.ORGGEOCHEM.2012.03.012>.
- Zhang, Y., Hu, A., Xiong, P., et al., 2022. Experimental study of temperature effect on methane adsorption dynamic and isotherm. *Energies* 15, 5047. <https://doi.org/10.3390/en15145047>.
- Zhou, W., Zhang, Z., Wang, H., et al., 2019. Molecular investigation of CO<sub>2</sub>/CH<sub>4</sub> competitive adsorption and confinement in realistic shale kerogen. *Nanomaterials* 9 (12). <https://doi.org/10.3390/NANO9121646>.
- Zou, J., Rezaee, R., Liu, K., 2017. Effect of temperature on methane adsorption in shale gas reservoirs. *Energy Fuels* 31, 12081–12092. [https://doi.org/10.1021/ACS.ENERGYFUELS.7B02639/ASSET/IMAGES/EF-2017-02639H\\_M014.GIF](https://doi.org/10.1021/ACS.ENERGYFUELS.7B02639/ASSET/IMAGES/EF-2017-02639H_M014.GIF).
- Zou, J., Rezaee, R., Xie, Q., et al., 2019. Characterization of the combined effect of high temperature and moisture on methane adsorption in shale gas reservoirs. *J. Petrol. Sci. Eng.* 182. <https://doi.org/10.1016/j.petrol.2019.106353>.